11-16-2022

Most Recent Rupture on the Boulder Creek Fault Triggered Bedrock Landsliding in the Nooksack Watershed, Whatcom County, Washington

Abigail Catherine Underwood
Portland State University

Most Recent Rupture on the Boulder Creek Fault Triggered Bedrock Landsliding in the Nooksack Watershed, Whatcom County, Washington

by

Abigail Catherine Underwood

A thesis submitted in partial fulfillment of the
requirements for the degree of

Master of Science
in
Geology

Thesis Committee:
Adam Booth, Chair
Ashley Streig
John Bershaw

Portland State University
2022

Abstract

Catastrophic bedrock landslides with volumes ranging from 10^6 to 10^8 m^3 contribute to rapid landscape evolution, often resulting in erosion rates that exceed the long-term average rates caused by tectonic uplift. Understanding the spatiotemporal trends of large bedrock landslides helps us understand previous drivers of landscape evolution as well as predict how the landscape will respond in the future. The Nooksack watershed, Whatcom County, Washington, is particularly susceptible to large slope failures because of its high relief, seismic activity, local geology, and relatively abundant precipitation. Specifically, folded and faulted bedrock structures conducive to landsliding in addition to recent surface rupturing earthquakes on the Boulder Creek fault are both probable mechanisms for widespread landsliding. To determine the relative importance of these driving mechanisms, we investigate spatiotemporal trends of 447 landslides in the Nooksack Watershed using a calibrated relationship between lidar based surface roughness and age. We compare the temporal patterns in the overall landslide chronology to simulated landslide frequency histories with and without incorporated coseismic landslide pulses at the times of the two most recent earthquakes on the Boulder Creek fault. We assess spatial patterns by conducting a regional kinematic analysis to define areas susceptible to planar sliding and toppling failures. We find surface roughness values of bedrock landslides in Washington's Cascade Range are consistent with roughness values determined for bedrock landslides in the Oregon Coast Range. Our resulting landslide frequency history best matches a simulated landslide frequency history that incorporates preservation bias as well as coseismic landslide pulses at the times of geologically constrained surface rupturing earthquakes on the Boulder Creek fault in the last 4000

years. Our regional kinematic analysis demonstrates almost half the landslides in our inventory overlay hillslopes where planar sliding and/or flexural toppling are kinematically feasible. These findings together support the conclusion that surface rupturing earthquakes and bedrock orientations, specifically those conducive to flexural toppling, primarily control the spatial and temporal distributions of landslides throughout the Nooksack watershed. These findings are important for hazard assessment and planning throughout the region and suggest the evolution of the Nooksack watershed is heavily influenced by coseismic landslides.

Acknowledgments

I would like to particularly thank my advisor, Adam Booth, for his unwavering support throughout my graduate studies, for sharing his enthusiasm for the topic with me and providing valuable feedback. I am grateful to have had the opportunity to learn from and work with Alison Duvall, Sean LaHusen, and Erich Herzig, who encouraged great discussion and provided me with code to aid in analyzing my results. I'd like to acknowledge and thank my thesis committee: Ashley Streig for always pushing me to think in complex ways and guiding me towards a bright future, as well as John Bershaw for being a positive influence and offering constructive comments to improve my final draft. A special thanks to the folks at WA-DNR for creating the several databases I used in this study, especially the landslides team who published the Whatcom County landslide inventory that served as a backbone for this research.

Thank you to my field assistants and great friends of mine, Zoie Yetley and Adrienne Stephens; obtaining samples would not have been possible without their help. I would also like to extend my gratitude to my cohort for their endless support and encouragement from the start of my graduate studies. A huge thank you from the bottom of my heart to my family and great friends who listened to me ramble about landslides in the Nooksack Watershed for two years, I couldn't have gotten where I am today without their endless support.

Funding from NSF Award 2000188 to Adam M. Booth, Alison R. Duvall, and Erin Wirth supported this research.

Table of Contents

Abstract....i
Acknowledgements....iii
List of Tables....v
List of Figures....vi

1.0 Introduction....1
2.0 Study Area and Background....6
2.1 Study Location....6
2.2 Tectonic Framework....7
2.3 Geologic Framework....8
2.4 Previous Age-Roughness Models....10
3.0 Material and Methods....13
3.1 Radiocarbon Ages....13
3.2 Landslide Inventory and Geomorphic Mapping....18
3.3 Quantifying Deposit Surface Roughness....20
3.3.1 Deposit Preparation....20
3.3.2 Roughness: Two-Dimensional Continuous Wavelet Transform....21
3.4 Modelling Landslide Frequency Histories....23
3.5 Regional Kinematic Analysis....24
4.0 Results....26
4.1 New Landslide Ages from Radiocarbon Dating....26
4.2 Pacific Northwest Bedrock Landslide Age-Roughness Model....29
4.3 Western Whatcom County Landslide Chronology....31
4.4 Susceptibility to Planar Sliding and Flexural Toppling....35
5.0 Discussion....36
5.1 Hazard Implications....36
5.2 Sources of Uncertainty....39
6.0 Conclusion....44
References....46

Appendix A. The Oso Landslide....53
Appendix B. The Deforming Cascadia Forearc....54
Appendix C. Field Work – Sampling....55
Appendix D. Two-Dimensional Mexican hat wavelet....57
Appendix E. Landslide Failure Styles....58
Appendix F. Oregon Coast Range Mean Roughness Values (LaHusen et al., 2020)....59

List of Tables

Table 1. Absolute landslide ages obtained from previous studies.....17

Table 2. New absolute ages of three landslides in Washington's Cascade Range.....28

Table 3. Mean roughness values for landslide deposits of known age in Washington's Cascade Range.....30

List of Figures

Figure 1. Tectonic setting and geography of study area.....5

Figure 2. A) Landslide deposits within the study are and B) Generalized geology of the study area.....9

Figure 3. Bald Mountain landslide sampling locations and field photos.....16

Figure 4. Locations of the landslides of known age used in the age-roughness model.....18

Figure 5. Example of original and modified landslide deposit polygons.....21

Figure 6. Pacific Northwest bedrock landslide age-roughness model.....30

Figure 7. Histogram of landslide ages for the past 32,000 years and B) Comparison of observed versus simulated landslide frequency histories for the past 4000 years.....33

Figure 8. A) Location of 93 landslides with ages between 768-1234 y.b.2019 and B) Areas susceptible to planar sliding and flexural toppling determined by our regional kinematic analysis.....34

Figure 9. ShakeMap of a scenario M6.8 earthquake on the Boulder Creek Fault.....38

1.0 Introduction

High-relief mountain ranges are in constant battle with the forces of erosion. Outside of wind and frequent freeze and thaw cycles, other agents of erosion such as precipitation in the form of snow or rainfall coupled with threshold slopes, or hillslopes near their angle of repose, make a recipe for mass wasting events. The latter ingredients, in addition to earthquakes, often result in large, catastrophic bedrock landslides with volumes ranging from 10^6 to 10^8 m^3 (Catastrophic Landslides of the 20th Century – Worldwide, https://www.usgs.gov/programs/landslide-hazards/science; Wartman et al., 2016). Landslides of this magnitude contribute to rapid landscape evolution by rapidly denuding slopes and regulating the size, amount, and longevity of sediment delivered to river channels (Booth et al., 2017). This can result in transient erosion rates that exceed the long-term average rates caused by tectonic uplift, emphasizing the important contribution landslides have on landscape evolution (Kelsey, 1978; Hovius et al., 1997; Malamud et al., 2004b; Blodgett and Isacks, 2007; Parker et al., 2011; Larsen and Montgomery, 2012; Booth et al., 2013). Better constraining the spatiotemporal trends of large-catastrophic landslides is essential to understanding previous drivers of landscape evolution as well as predicting how the landscape will respond in the future.

Mechanisms responsible for decreasing slope stability can occur over multiple time scales (Caine, 1980; Keefer, 1984; Schmidt and Montgomery, 1995; Bilderback et al., 2014; Gischig et al., 2015). In general, a landslide will occur when a slope's shear strength drops below the driving shear stress acting on the failure plane. The frictional strength of a hillslope is controlled by the effective normal stress, defined as the normal stress minus the pore water pressure. Intense rainfall events responsible for increasing

pore water pressure may decrease the effective normal stress, leading to slope instability (Caine, 1980). Earthquake generated ground movements may also reduce the effective normal stress acting on a hillslope by rapidly compacting sediments resulting in elevated pore pressures. Pore water pressures aside, ground accelerations may also simply increase the driving stress or reduce the normal stress, causing slope failures (Keefer, 1984). Although the latter processes predominantly occur over shorter timescales, long term strength loss from weathering processes, increased pore water pressure in response to changes in climate (Bilderback et al., 2014), and/or recurrent damage to bedrock from earthquakes can also jeopardize hillslope stability (Gischig et al., 2015). Where rock slopes are in a sufficiently critical state from repeat seismic loading, even small pore pressure increases associated with ordinary seasonal water cycles or a minor earthquake may be enough to trigger catastrophic failure (Gischig et al., 2015). Other tectonic related processes occurring over millennia are responsible for generating swaths of folded and faulted bedrock, predisposing hillslopes for failure on geologic structures. Folded and faulted heterogenous lithologies within a hillslope also affect hydraulic conductivities and the associated groundwater flow fields, which can locally elevate pore water pressures and initiate failure (Guglielmi et al., 2005; Jomard et al., 2010). As tectonic uplift continues, hillslopes become more susceptible to failure as base level drops and subsequent river incision produces topographic relief, increasing a hillslope's driving stress (Schmidt and Montgomery, 1995). Although we have general knowledge of the mechanisms responsible for hillslope failures, pinpointing the predominant failure mechanisms and triggers throughout a region remains a challenge.

Certain regions throughout the world have higher landslide hazard than others, especially those with steep topography and frequent rainfall, and those located on tectonically active margins. Globally, regions overlaying subductions zones typically contain all these characteristics. The tectonic plate movement associated with subduction often results in large magnitude earthquakes along the interface of the two plates as well as smaller magnitude earthquakes associated with crustal shortening and uplift inland of the plate interface. Landslides associated with intense ground shaking are earthquakes' greatest secondary hazard, and can exceed the damages strictly related to the earthquake, such as in the case of the January 2001 El Salvador earthquake or the 1987 Ecuador earthquake (Bird and Bommer, 2004; Marc et al., 2016). In remote areas, coseismic landslides may not have an immediate effect on society, but floodwaters from breached landslide dams carry the potential to damage distant infrastructure downstream (Fan et al., 2020).

To determine the catalysts of large prehistoric, deep-seated, bedrock landslides, or landslides that fail beneath the rooting depth of trees (~2 m), we must first understand their spatiotemporal distribution, which is traditionally accomplished by creating a landslide inventory. Accurate inventories rely on high-resolution lidar (light detection and ranging) data, especially in areas where the bare earth surface is obscured by dense vegetation (Schulz, 2007). Despite the usefulness of high-resolution lidar data for creating landslide inventories that are used to determine susceptibility, hazard, vulnerability, and risk, they often lack age information (LaHusen et al., 2020). Landslides are most commonly dated using radiocarbon analyses or dendrochronology. However, these techniques are not feasible at regional scales due to expenses, limited access to

landslide deposits, and the lack of datable material within deposits (Pánek, 2014). Recent studies in the Oregon Coast Range and the North Fork Stillaguamish River Valley, Washington state, have shown that landslide deposit surface roughness measured from lidar can be used as a proxy for landslide age to construct regional landslide chronologies with a limited number of absolute ages (LaHusen et al., 2016, 2020; Booth et al., 2017).

Here, we calibrate and apply a surface roughness dating model to 447 deep-seated bedrock landslides in the Nooksack River watershed, Whatcom County, Washington (figure 1). With potential seismic, climatic, and base level triggers at play in northwestern Washington, we investigate spatiotemporal trends in landsliding to determine their primary driving mechanism(s). Better understanding what causes these landslides will shed light on how the landscape responds to specific triggers in the context of long-term landscape evolution. The more practical results of this research are crucial for hazard assessments and risk evaluations as populations continue to increase in areas more exposed to landslides.

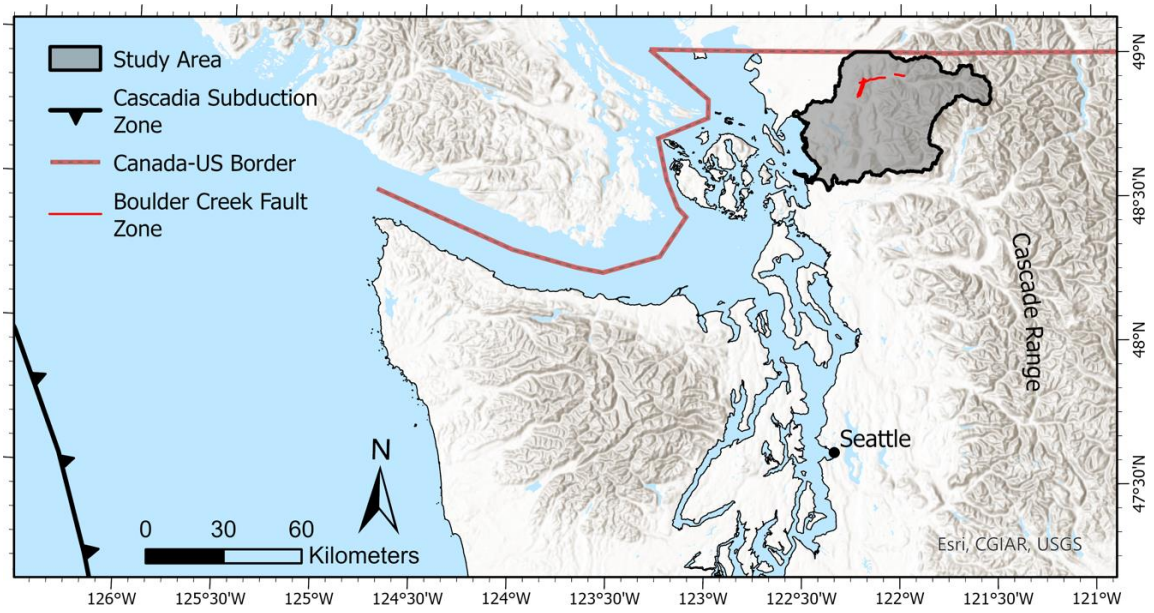

Figure 1. Tectonic setting and geography of study area. Polygon outlined in black and shaded gray depicts extent of the study area, defined as the eastern two thirds of the Nooksack Watershed and a few smaller adjacent watersheds. The Cascadia Subduction Zone runs roughly north-south ~300 km to the west of the study area. Crustal faults in the Boulder Creek Fault Zone are shown as red lines in north-central portion of the study area.

2.0 Study Area and Background

2.1 Study Location

The Pacific Northwest (PNW), United States is prone to extensive landsliding due to the combination of regional tectonic setting and climatic conditions. Washington, specifically, is situated on an active convergent margin where the Juan de Fuca plate is subducting beneath the North American plate. The resulting folded and faulted bedrock formations in addition to frequent large rainfall events contribute to the hundreds to thousands of landslides each year, making it one of the most landslide prone states in the country. Landslide studies in Washington have increased following the devastating Oso landslide in 2014 (Iverson et al., 2015; Wartman et al., 2016; Stark et al., 2017; Collins and Reid, 2019). This landslide was the deadliest landslide in the history of the continental United States, claiming the lives of 43 people as it rapidly inundated the Steelhead Haven community (figure S1) (Wartman et al., 2016). From shallow failures to catastrophic large, long run-out, deep-seated landslides like the Oso landslide, these geologic hazards are a persistent risk to communities and infrastructure throughout Washington. Despite their prevalence, the relative importance of various mechanisms responsible for deep-seated bedrock landslides throughout Washington remains generally unclear, meriting further research efforts to better inform mitigation plans.

This study focuses on the Nooksack Watershed, Whatcom County, Washington, which lies between Skagit County and the United States-Canada border and is particularly susceptible to large slope failures because of its high relief, seismic activity, and relatively abundant precipitation (figure 1) (Brunengo, 2001). Paleoseismic studies

reveal several crustal faults within or adjacent to Whatcom County have ruptured at similar times throughout the Holocene, possibly triggering coseismic landsliding. Its high susceptibility coupled with high population density and dense infrastructure warranted landslide mapping by the Washington Department of Natural Resources (WA-DNR), which documented 1,911 landslides over a ~3620 km^2 region in western Whatcom County (Mickelson et al., 2020). A subset of that landslide inventory consisting of large bedrock landslides was used in this study (figure 2A).

2.2 Tectonic Framework

On the North American plate, the Sierra Nevada microplate is colliding into southern Oregon, resulting in continuous northward progression and clockwise rotation of the Cascadia forearc relative to stable North America (figure S2) (Wells and Simpson, 2001). The Canadian Coast Mountains act as a rigid backstop, causing the northern forearc, between Olympia, Washington and the US-Canadian border, to shorten at a rate of approximately 4-7 mm/yr (Wells and Simpson, 2001; Kelsey et al., 2012; Sherrod et al., 2013). Here, systems of crustal faults are thought to accommodate much of the resulting strain (Kelsey et al., 2012), as evident in GPS measurements and paleoseismic studies (Wells and Simpson, 2001; Kelsey et al., 2012).

In the study area, the Boulder Creek fault zone (BCFZ) partially comprises the northern leading edge of the deforming Cascadia forearc and is also thought to accommodate north-south shortening (figure 2A-B) (Kelsey et al., 2012). In the BCFZ, lidar reveals a scarp on the mapped trace of the Boulder Creek Fault (BCF) and another along a fault near Canyon Creek (Sherrod et al., 2013; Sherrod and Gomberg, 2014). Four trenches across the scarp of the BCF, one trench across the scarp near Canyon

Creek, and plant remains from a scarp-dammed wetland along the BCF reveal three distinct ruptures throughout the Holocene, with the most recent surface rupturing earthquake occurring between 1165 and 699 cal. years before present (1950) (yrs B.P.), a penultimate earthquake occurring between 2990 and 3344 cal. yrs B.P., and an antepenultimate earthquake occurring ~7700 cal. yrs B.P. (Barnett, 2007; Sherrod et al., 2013; Sherrod and Gomberg, 2014).

2.3 Geologic Framework

Whatcom County is underlain by complex geology that can be divided into three broad categories: Quaternary deposits, Tertiary rocks, and pre-Tertiary rocks (figure 2B). The youngest deposits represent packages of unconsolidated Quaternary post-glacial and Pleistocene glacial sediments from the most recent ice-sheet glaciation, the Fraser Glaciation (Lapen, 2000). Radiocarbon dates constraining the Fraser glaciation in the Pacific Northwest correspond with the mid-continent Wisconsin glaciation, at ~25-10 kya (Booth et al., 2003). Sedimentary rocks from the Tertiary have been uplifted and are found in the Chuckanut and Huntingdon formations. The Chuckanut formation is divided into seven members, ranging in age from late Paleocene to early Oligocene. These rocks consist mostly of sandstone, siltstone, conglomerate, and coal and are interpreted as the result of a strike-slip pull apart basin with subsequent filling from local uplifts and distant sources (Lapen, 2000). The Huntington formation contains moderately well sorted conglomerates, sandstones, siltstones, shales, and clays with ages correlative to strata of the Chuckanut Formation (Lapen, 2000). Pre-tertiary rocks in the Nanaimo group, consist of upper Cretaceous sandstone, conglomerate, shale, and minor coal from four typical transgressive cycles (Lapen, 2000). Various sheared and deformed metamorphic,

volcanic, metasedimentary, and metaigneous rocks of the Chilliwack Group of Cairnes, Nooksack Formation, and Cultus Formation of the northwest Cascade system are also present and range in age from Jurassic to pre-Devonian (figure 2B) (Lapen, 2000; Tabor et al., 2003).

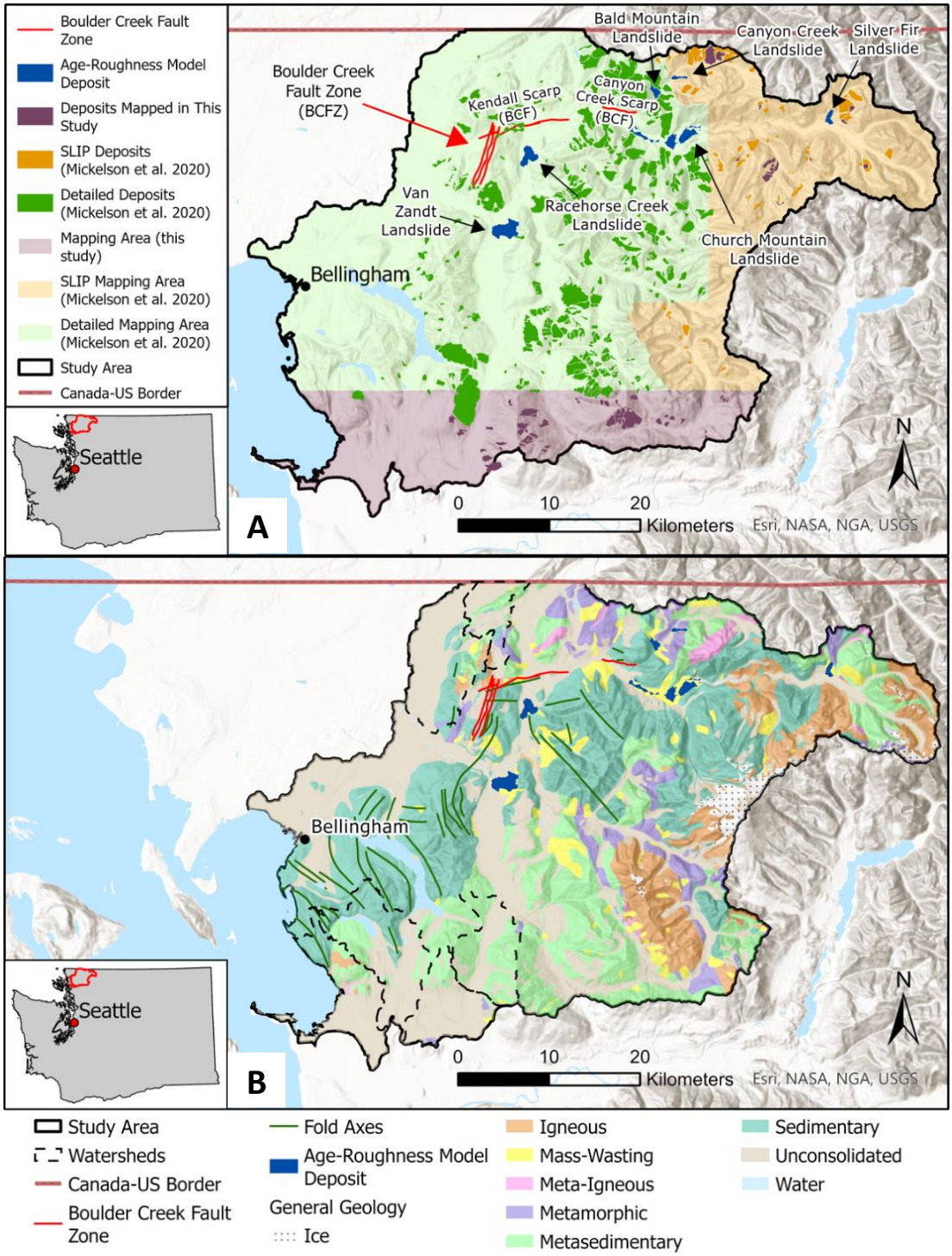

Figure 2. A) Landslide deposits within the study area. Dark green polygons indicate deposits mapped in detail by WA-DNR. Orange polygons indicate deposits mapped by WA-DNR (Mickelson et al., 2020), following the SLIP protocol (Slaughter et al., 2017). Purple polygons indicate deposits we mapped in detail. Blue polygons indicate five of the eight deposits used in our age-roughness model: the Racehorse Creek and Church Mountain landslides, dated by Pringle et al. (1998), the Van Zandt landslide, dated by Malick (2018), and the Silver Fir and Bald Mountain landslides, dated in this study. The Canyon Creek landslide was dated in this study was but not used in our age roughness model. The remaining three deposits used in the model do not fall within the extent of our study area boundaries (see section 3.1 and figure 4). **B) Generalized geology of the study area**. Holocene active faults within the study area represented as red lines and folds as green lines. The eastern most portion of the Nooksack Watershed makes up 1899 km^2 of the study area and the smaller surrounding watersheds account for the remaining 420 km^2.

The complex geology underlaying Whatcom County is important to understand when assessing landslide driving mechanisms. In general, pre-existing geologic structures including foliation, faults, fractures, and bedding plane orientation control the style of landsliding on a bedrock slope (Hermanns and Strecker, 1999; Brideau et al., 2005; Ganerød et al., 2008; Booth et al., 2014). Landslides in sedimentary units are often controlled by bedding plane orientation, where depositional contacts between steeply dipping strata resulting from folding and faulting events exhibit low shear strength (Roering et al., 2005). If those weak planes dip more steeply than the friction angle and project out of the topographic slope, a dip-slope landslide, or planar sliding, is possible. Additionally, sub-vertical joints and faults and/or bedding planes often result in forward toppling. Overall, a weak unit within a stratigraphic sequence may result in deep-seated landsliding, emphasizing the importance of understanding the lithologies within a hillslope (Roering et al., 2005).

2.4 Previous Age-Roughness Models

Previous studies have demonstrated surface roughness can be measured from high-resolution topographic data to generally reflect several properties of a landslide such

as size, activity, type, and material properties (McKean and Roering, 2004; Glenn et al., 2006; Booth et al., 2009; Berti et al., 2013). Because landslides display higher roughness values than surrounding stable terrain, they can be quantitatively distinguished on lidar derived hillshade and slope maps. Younger landslides have high roughness values resulting from large, displaced blocks, hummocks, and closed depressions. Older landslides tend to have a more subdued topographic signature as erosional processes and soil diffusion have more time to rework and smooth the deposit's morphology (Keaton and DeGraff, 1996; Booth et al., 2017). Although the idea of using surface roughness as a method to generally quantify properties of a landslide has been demonstrated in several prior studies, until 2014, none had investigated the accuracy of quantifying surface roughness as a proxy for landslide age (Goetz et al., 2014). Goetz et al. (2014) conducted an age-roughness study in the Swabian Alb, Germany. They used three different measures of surface roughness over a ~200-year timespan and found little to no correlation between landslide age and deposit surface roughness. However, they suggested lithologic variation and landslide reactivation may have obscured the age-roughness relationship due to their small sample size of 12 landslides and short period of analysis. LaHusen et al. (2016) and Booth et al. (2017) revisited the idea and established a significant correlation between landslide age and deposit surface roughness to estimate the ages of more than 200 landslides occurring in glacial sediments of the North Fork Stillaguamish River Valley, Washington, throughout the Holocene. LaHusen et al. (2020) took this concept a step further and used age-roughness analysis to gain insight into the driving mechanisms of bedrock landslides in the Oregon Coast Range (OCR). Here, they estimated the ages of 9,938 bedrock landslides, and found that locations of bedrock

landslides in the OCR are significantly correlated with mean annual precipitation, but timing was not related to Cascadia subduction zone (CSZ) earthquakes. Because the bedrock, climate, and proximity to faults capable of producing large magnitude earthquakes are broadly similar in the Nooksack watershed we use the LaHusen et al. (2020) study as the framework for our research. We gathered and obtained the ages of a limited number of landslides in Washington's Cascade Range to create an age roughness model and investigated the spatiotemporal trends of landslides in Nooksack Watershed in Whatcom County, WA.

3.0 Material and Methods

3.1 Radiocarbon Dating

An essential component to creating an age-roughness model is obtaining absolute ages of a limited number of landslides where lidar is also available to quantify deposit roughness. We gathered the absolute ages of six bedrock landslides in Washington's Cascade Range (WCR) from previous landslide studies (table 1). Pringle et al. (1998) refined the ages of eight landslides in the WCR using radiocarbon dating, four of which are located in regions with available lidar data: the Church Mountain, Racehorse Creek, Damnation Creek, and Day Lake landslides (figures 2A and 4 and table 1). Despite not being in our study area, we use the age of the Damnation Creek landslide, ~50 km southeast of our study area, and the Day Lake landslide, ~50 km south of our study area, because they are in regions with similar topographic, lithologic, and climatic settings. Additionally, we use the age of the Bonneville landslide on the Columbia River, ~350 km south of our study area, which has been refined through several studies that used radiocarbon analyses, dendrochronology, and lichenometry, making it a strong anchoring data point for our age-roughness model (figure 4) (Pringle et al., 1998, 2021; Pringle, 2009; Reynolds et al., 2015).

In our study area, Malick (2018) dated the Van Zandt landslide. This landslide complex is comprised of three lobes, two of which are thought to have occurred simultaneously (Malick, 2018). For our age-roughness model, we use the radiocarbon age data from this study that best describes the simultaneous emplacement of the two lobes to define the age of the Van Zandt landslide (table 1 and figures 2A and 4) (Malick, 2018).

Additionally, we determined the ages of three landslides within the study area: the Silver Fir, Bald Mountain, and Canyon Creek landslides (section 4.1) (table 2 and figures 2A and 4). We targeted large landslides that ran out into river valleys, where rivers were actively eroding the landslide toe, revealing fresh exposures of the deposit (figure 3A). We sampled logs at these sites assuming they were killed at the time of the landslide, entrained within the deposit, and subsequently exposed by erosion along river cutbanks (Pánek, 2014). However, fluvial processes can wedge logs into river cutbanks, and/or trees can fall on older landslide deposits and be buried by soil horizons or additional mass wasting processes, which would post-date the landslide. To minimize the likelihood of obtaining ages younger than or otherwise unrelated to the landslide, we followed a set of three criteria. Most importantly, the log or wood fragment must be within the landslide deposit, which we determined based on the presence of angular, poorly sorted, gravel to cobble sized clasts within a matrix of well compacted muds and clays (figure 3B-C). These deposits contrasted with fluvial deposits containing imbricated or rounded gravels and/or cobbles. Where logs protruded from the deposit, we made sure they projected far back into the deposit, roughly perpendicular to the riverbank face, making them unlikely to have been wedged against the bank by fluvial processes. In any case where there was more than one log protruding from the deposit, we sampled the stratigraphically lowest log to avoid the chance that it may be a fallen tree or from a later mass wasting event. Obtaining a sample from an organic source that was mobilized in the landslide event of interest would result in a maximum age, while any sample source embedded in a reactivation after the larger, main event, would result in a minimum age.

We collected multiple samples from the Silver Fir, Bald Mountain, and Canyon Creek landslides, and later decided on the two best samples from each based on the criteria above (figures 2-4, figures S3 and S4, and table 2). We cleaned the samples of sediment and other organic material with deionized water and dried the samples in the oven at a 50° C for 24+ hours before sending them to the National Ocean Sciences Accelerator Mass Spectrometry (NOSAMS) facility for radiocarbon dating. Upon receiving results, we used OxCal (Bronk Ramsey, 2009) to calibrate the radiocarbon ages to years before 1950 (yrs B.P.) and years before 2019 (y.b.2019) to compare to LaHusen et al. (2020).

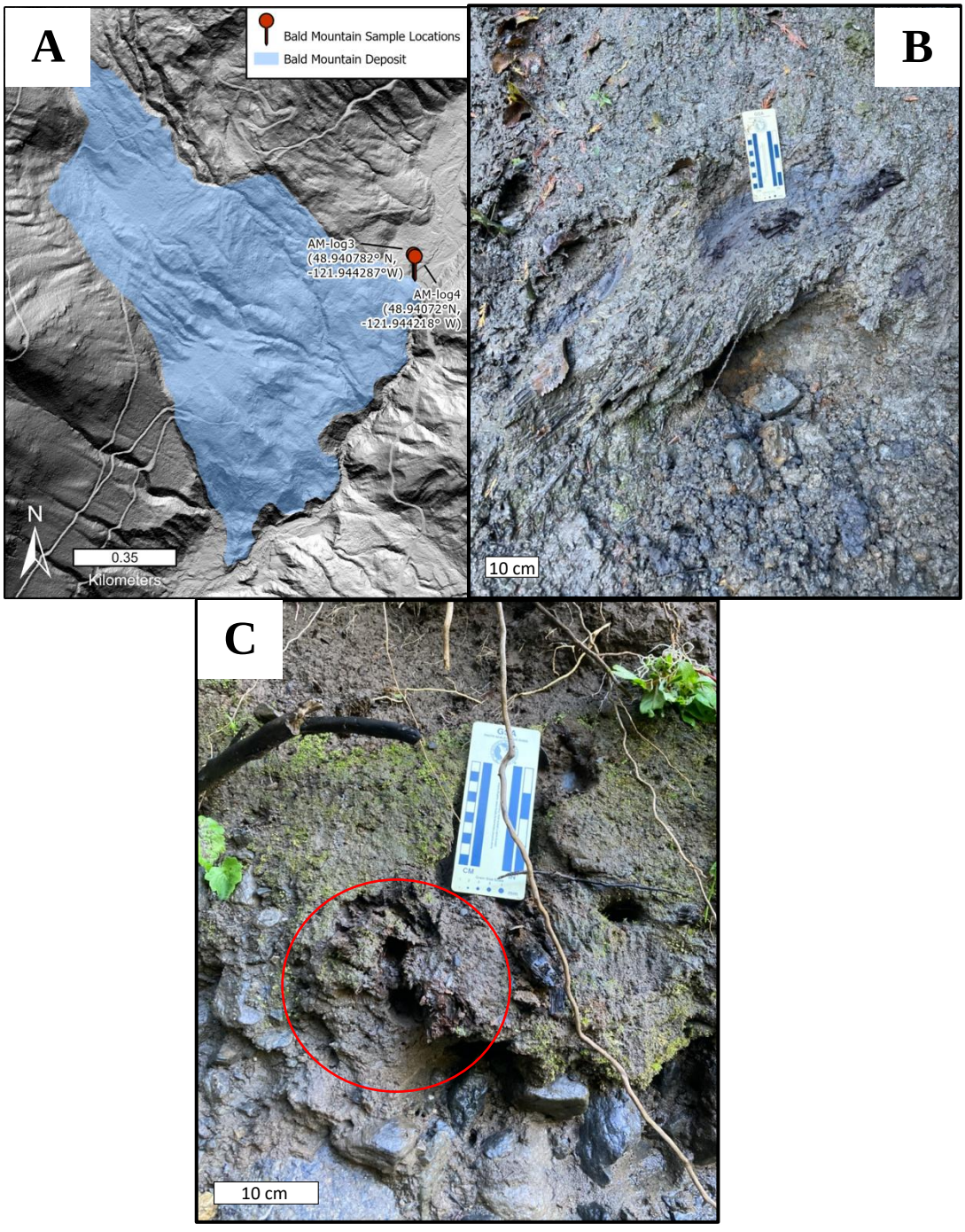

Figure 3. Bald Mountain landslide sampling locations and field photos. A) Blue deposit polygon for the Bald Mountain landslide draped over a hillshade map derived from ~0.9m bare earth lidar imagery obtained from WA-DNR's lidar portal. Sample locations are denoted as red pins with the corresponding sample name and GPS coordinates labeled accordingly. **B)** Heavily deteriorated log we obtained sample AM-log4 from. Note the heavily compacted clays encasing this log. **C)** Below the GSA scale and circled in red is the small, moderately deteriorated log protruding from deposit that we obtained sample AM-log3 from. See appendix C for Silver Fir and Canyon Creek sampling locations.

Table 1. Absolute landslide ages obtained from previous studies

Landslide Name	Calibrated Age (years B.P.)*	Calibrated Age (years before 2019)***	Source of Sample	Reference
Church Mountain Landslide	2414 ± 315	**2483**	Sample from outer 10 rings under bark of cedar log lying under CMA-92-2	Pringle et al. (1998)
Day Lake Landslide	1540 ± 195	**1609**	Sample from 90-cm diameter snag in Day Lake; estimated >100 rings missing?	Pringle et al. (1998)
Racehorse Creek Landslide	4234 ± 390	**4303**	Sample from innermost 10 rings of cedar log having about 65 rings and buried in silt under Racehorse Creek rockslide deposit.	Pringle et al. (1998)
Damnation Creek Landslide	7839 ± 130	**7908**	Organic horizon in lacustrine silt upstream of rockfall and under Mazama ash.	Pringle et al. (1998)
Van Zandt Complex	1300 ± 30	**1369**	Terminal growth ring of in situ log with bark.	Malick (2018)
Bonneville Landslide	504**	**573**	Submerged forest trees near the shore at Wyeth and Perham Creek and a bark-bearing log exhumed from the landslide deposit during excavations for Bonneville's second powerhouse in 1978.	Pringle et al. (2021)

*Calibrated years before present is before 1950 written as the median ± 2 standard deviations.

**Bonneville landslide was precisely dated to late 1446 or early 1447 CE

***Age used in age roughness model

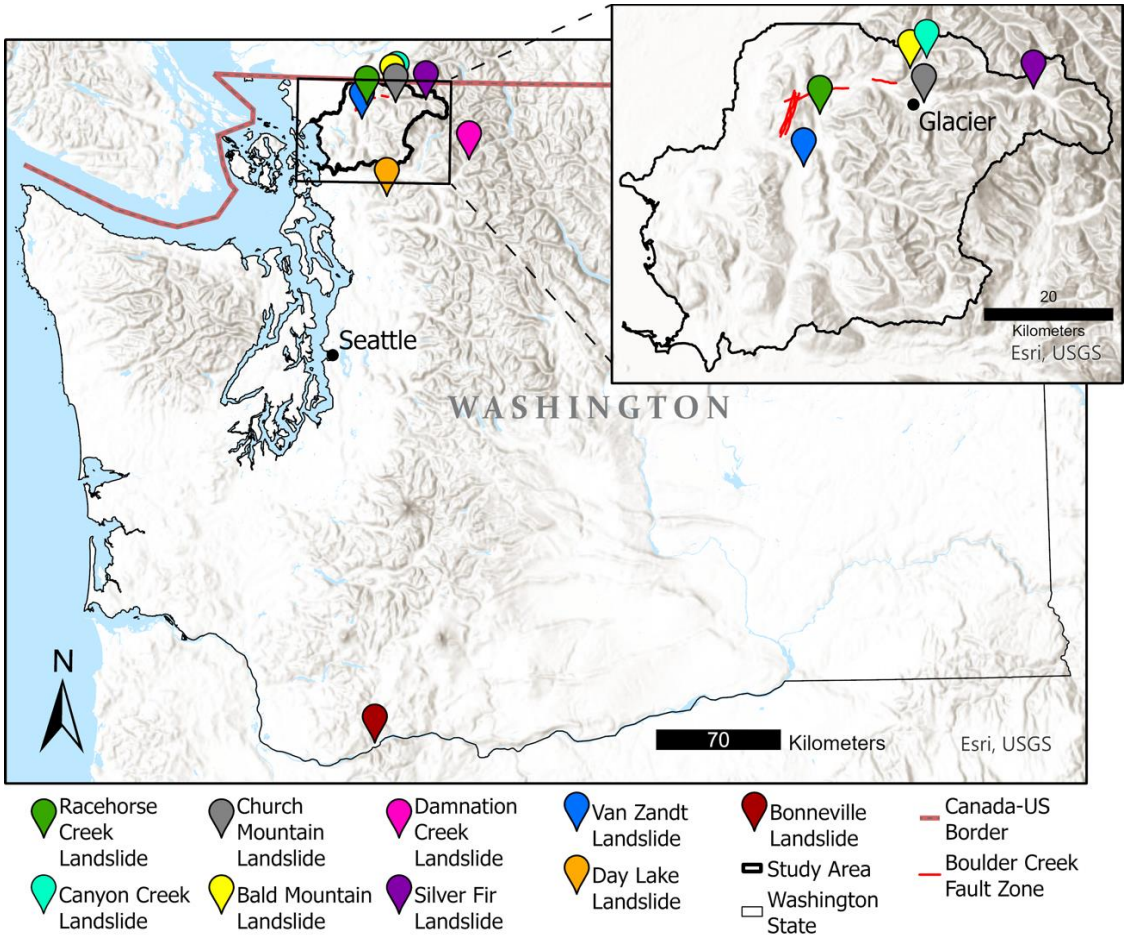

Figure 4. Locations of the landslides of known age used in the age-roughness model. Landslide ages and references shown in Table 1 and age results for the Silver Fir, Bald Mountain, and Canyon Creek landslides shown in Table 2. The Canyon Creek landslide was not used in our age roughness model (section 4.1).

3.2 Landslide Inventory and Geomorphic Mapping

For our landslide inventory, we modified and expanded upon an existing landslide inventory for part of Whatcom County, Washington (Mickelson et al., 2020). In that inventory, 1,587 of the 1,911 landslides were mapped in detail following the mapping protocol of Slaughter et al. (2017), a modification of the protocol developed by Burns and Madin (2009). The detailed mapping focused on areas with dense populations and infrastructure, digitizing landslide landforms including deposits, scarps, flanks, and any

internal scarps. The remaining 324 landslides were mapped following the Slaughter et al. (2017) Streamlined Landslide Inventory Protocol (SLIP), which only included a singular polygon depicting the entire landslide (a combination of the deposit, scarps, and flanks). The area mapped following the SLIP protocol focused on generally unpopulated areas that may contain significant infrastructure and is less complete than the detailed mapping area (figure 2A).

We first revised the existing inventory based on a set of criteria we hypothesized would produce the best results for quantifying surface roughness. Since our age-roughness model is derived from deep-seated, bedrock landslides, we eliminated landslides occurring in unconsolidated sediments as well as landslides characterized as shallow flows within the soil column. To distinguish deep-seated, bedrock landslides from shallow flows, we omitted landslides with headscarps less than 2 meters. This criterion is important as shallow, channelized earth/debris flows, or any landslide occurring in unconsolidated sediments exhibit different failure morphologies than bedrock landslides and may therefore be inappropriate to include in our analysis. Additionally, we applied a minimum size threshold of 93,000 m^2 to ensure the landslide deposits were large enough to exhibit characteristic roughness (section 3.2). Filtering the existing landslide inventory with these criteria decreased the number of landslides for our analysis from 1,911 to 392.

To complete the inventory for our study area, following Slaughter et al. (2017), we mapped an additional 41 landslides in a 378 km^2 area where watersheds crossed the Whatcom County boundary that defined the map extent for Mickelson et al. (2020). In the SLIP mapping area, we mapped an additional 14 landslides for a more complete

inventory, following the same criteria defined above (figure 2A). DEMs and lidar data used for mapping were acquired from WA-DNR's lidar portal.

3.3 Quantifying Deposit Surface Roughness

3.3.1 Deposit Preparation

To define the average surface roughness of each landslide, we further modified the inventory to isolate portions of landslides where natural soil transport processes would smooth the surface over time. Most importantly, we isolated deposits from their head and side scarps, as well as removed any other features that would bias their overall roughness. Landslides mapped following the SLIP protocol (Slaughter et al., 2017) were modified to isolate the deposit from the generalized polygon. We began modifying each deposit polygon by first applying a 20 m buffer to avoid edge effects of deposit boundaries. Then, river cutbanks, stream gullies, ponds, reactivations, roads, and/or any anthropogenic structures or industrialized land were removed, also with a 20 m buffer (figure 5A-4B). This buffer size is the same as the length scale over which roughness was calculated (section 3.3.2). For the eight landslides used to define our age-roughness model, we manually removed the above-mentioned features to be as accurate as possible. However, manually removing streams and roads from all 447 deposits in our landslide inventory was not feasible. Instead, we derived and extracted the stream network by applying a drainage area threshold of 1,475 m^2, which was estimated visually by comparing the results of several drainage area thresholds to the manually identified stream gullies, and then applied that to our entire study area. To remove roads, we used the WA-DNR database (Washington Department of Natural Resources, last edited 2022). Reactivations within larger landslide complexes, including their headscarps and side

scarps, were manually removed entirely from deposits if they were smaller than the 93,000 m^2 size threshold. If larger, they were mapped as their own unique landslide.

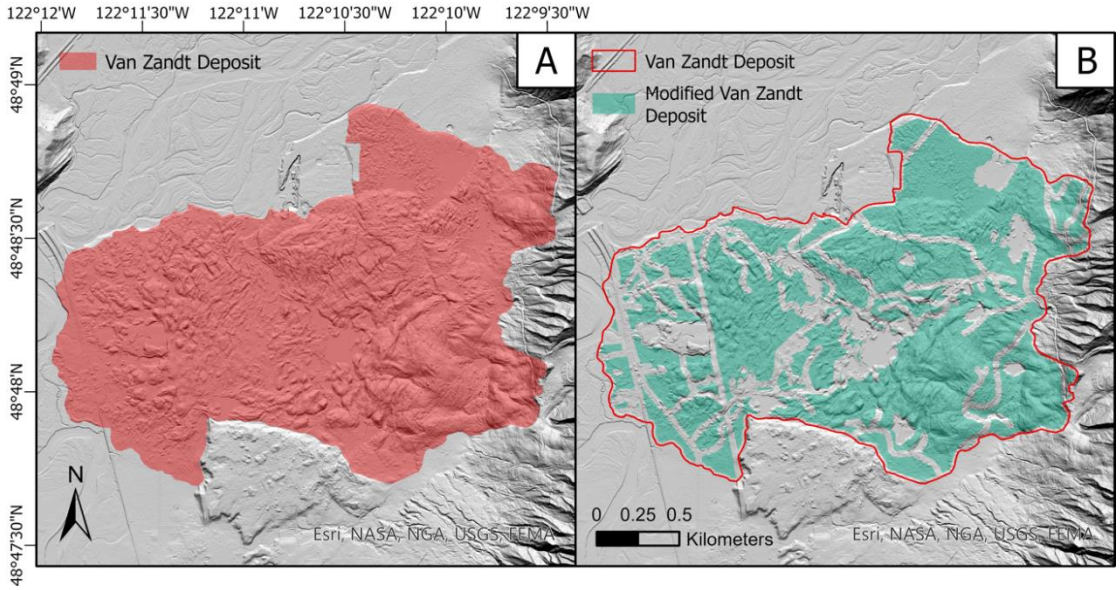

Figure 5. Example of original and modified landslide deposit polygons. A) The original landslide deposit polygon for the Van Zandt landslide. **B)** Van Zandt landslide deposit polygon modified to exclude edges, roads, river cutbanks, ponds, and other anthropogenic features with a 20 m buffer. The surrounding red line represents the extent of the original deposit polygon shown in A. Polygons are draped over hillshade maps derived from ~0.9 m bare earth lidar imagery obtained from WA-DNR's lidar portal.

3.2.2 Roughness: Two-Dimensional Continuous Wavelet Transform

Although different metrics and spatial scales can be used to quantify the topographic roughness of a landslide deposit, here we use the two-dimensional continuous wavelet transform (2D-CWT) with a 20 m Mexican hat wavelet to quantify the surface roughness of the 447 deposits in our inventory as well as the 8 landslides of known age for our age-roughness model (Booth et al., 2009) (figure S5). The best suited roughness metric and spatial scale often depend on characteristic morphologies of landslide deposits in the region. For example, a wavelet-based curvature measured at a 15 m spatial scale performed best at predicting absolute landslide ages of landslides in glacial deposits in the North Fork Stillaguamish river valley, while a 20 m spatial scale

performed best for bedrock landslides in the Oregon Coast Range (Booth et al., 2017; LaHusen et al., 2020). The difference in spatial scales from site to site likely reflects differing failure materials, as the landslides in the North Fork Stillaguamish river valley occurred in unconsolidated Quaternary post-glacial and Pleistocene glacial deposits, and the landslides in the Oregon Coast Range occurred in underlying sedimentary rocks in the Tyee and Elkton formations (Booth et al., 2017; LaHusen et al., 2020). The longer wavelength metric likely performs best in the Oregon Coast Range because the 20 m spatial scale better corresponds to the size of dominant roughness elements, such as hummocks and displaced blocks.

Generally, the 2D-CWT provides information regarding how amplitude is distributed over spatial frequency at each position in the data by transforming spatial data into position-frequency space (Booth et al., 2009) (figure S5). More specifically, it calculates topographic curvature at a specified smoothing length scale by convolving the wavelet kernel,

$$\psi = -\frac{1}{\pi(a\Delta)^4}\left(1 - \frac{x^2+y^2}{2a^2}\right)e^{-\frac{x^2+y^2}{2a^2}}, \quad (1)$$

where a is the wavelet scale, Δ is grid spacing, and x and y are spatial coordinates, with the DEM (Lashermes et al., 2007). The smoothing length scale is

$$\lambda = \frac{2\pi\Delta a}{\sqrt{5/2}} \quad (2)$$

(Torrence and Compo, 1998). The mean absolute value of the roughness (i.e. curvature measured at a 20 m smoothing length scale) for each landslide deposit was then extracted from all our mapped deposit polygons.

3.4 Modelling Landslide Frequency Histories

Using the ages we determined for all 447 landslides in our study area, we created landslide frequency histories for the past 32,000 and 4,000 years. We focused on the last 4,000 years to be able to accurately identify peaks that may represent periods of widespread landslide triggering due large earthquakes on the BCF that are otherwise not discernable in the 32,000-year age-frequency data. To test whether peaks in our age-frequency data represent coseismic landslide pulses associated with ruptures on the BCF, we simulated landslide frequency histories with and without earthquakes to compare to our dataset. To build the simulated chronology composed entirely of "background" landslides with no coseismic landslide pulses, we assigned a background rate of 0.2 landslides/year (20 landslides/century). This rate, after adjusting for preservation bias by multiplying the synthetic landslide frequency history with the same exponential decay function that fit our observed data, produced a total number of simulated landslides to have ages less than 4000 y.b.2019 roughly equal to the total number of observed: 397. For the simulated chronology with earthquakes, we generated two coseismic landslide pulses at the times of geologically constrained surface rupturing earthquakes on the BCF (section 2.2), each with 40, 60, 65, 67, and 80 slides per pulse, and determined 67 landslides per pulse best matched our observations. Because the model does not account for error margins associated with radiocarbon dating, we used the median age of the reported earthquakes in years before 2019 (1001 and 3236 y.b.2019) (Barnett, 2007; Sherrod et al., 2013; Sherrod and Gomberg, 2014). Here, we adjusted the background rate to 0.16 landslides/year so the total number of estimated landslides remained roughly equal to the total number of observed landslides with superimposed coseismic landslide

pulses. To account for the range of roughness values produced by landslides of the same age, we calculated the standard deviation (SD) of roughness values for the Van Zandt landslide and multiplied this value by two to address the uncertainty in calculating SD from a small sample. Using this SD, a randomly generated, normally distributed set of landslide roughness values was added at each model time step, where roughness values at each time step correspond to the time step age. We modeled each of these scenarios 10^4 times, and the ages were calculated for each run using the best fit age-roughness regression we used to calculate the ages of the 447 landslides in the Nooksack Watershed. Lastly, we calculated the mean frequency as well as the 10^{th} and 90^{th} bounding percentiles for all model runs.

3.5 Regional Kinematic Analysis

To test whether structural orientations of bedrock predominantly control the spatial pattern of landsliding throughout the study area, we conducted a regional kinematic analysis for planar sliding and flexural toppling (Norrish and Wyllie, 1996) (figure S6). We used 444 attitude measurements from the Chuckanut, Huntingdon, Nooksack, and Cultus Formations that we obtained from the 1:100,000 scale geologic mapping database of Washington State Digital Data to transform dip direction and dip angle point data into 30 m grids using inverse distance weighted interpolation (Washington Division of Geology and Earth Resources, 2016). We then compared these interpolated rasters to slope angle and slope direction (aspect) rasters derived from a 30 m DEM to identify areas where planar sliding and flexural toppling are kinematically feasible. We assumed a friction angle of 20° (Crider et al., 2009) and a maximum difference between dip and slope direction of 50° to define the failure windows. Unlike

typical kinematic analyses that focus on a singular or select few landslides, the resulting rasters display areas across the landscape that are susceptible to each of these types of failures (figure 8B).

4.0 Results

4.1 New Landslide Ages from Radiocarbon Dating

Using the OxCal v4.4.4 software online, we calibrated our radiocarbon ages to reflect sample age in cal. years before 1950 (yrs B.P.) and before 2019 (y.b.2019), consistent with LaHusen et al. (2020) (Bronk Ramsey, 2009) (table 2). Our calibrated ages reflect the median and uncertainty of the most likely age range with 95% confidence. For SilverFir-2, the radiocarbon age calibrates to 181 ± 44 cal. yrs B.P. We note this young age likely is the result of a recent reactivation just north of where we sampled. The radiocarbon age for SilverFir-6 calibrates to 1,959 ± 41 cal. yrs B.P. This sample was buried deeper in the deposit, and we interpret that this older age is more representative of the mapped landslide. Furthermore, the roughness of the deposit is similar to other previously dated landslides of similar age. Of the two samples for the Silver Fir landslide, we decided the age that best represents this landslide for our age-roughness model is sample SilverFir-6 with a median calibrated age of 2,028 y.b.2019 (table 2).

Results for the samples from the Bald Mountain landslide were similar. The calibrated ages for AM-log3 and AM-log4 were 83 ± 62 cal. yrs B.P. and 3,593 ± 45 cal. yrs B.P., respectively. We rule out the younger age as being representative of the mapped landslide deposit, as it likely reflects subsequent surficial erosion or shallow reactivation of the deposit. We therefore use 3,662 y.b.2019 as the absolute age of the Bald Mountain landslide in our age-roughness model (table 2).

For the Canyon Creek landslide, the calibrated ages for SGLR-6 and SGLR-10 are 43,899 ± 2,650 cal. yrs B.P. and 47,124 ± 4,925 cal. yrs B.P., respectively. The

radiocarbon ages for both samples here date back to the last glacial maximum, implying that the wood and deposit that contained it were remobilized by the landslide later. Though this landslide does not provide useful data for the age-roughness model, it provides us with an upper bounding limit for landslide age in our study area (table 2).

Table 2. New absolute ages of three landslides in Washington's Cascade Range

Landslide Name	Sample	Lab (NOSAMS) Accession #	Sample Coordinates	Radiocarbon Age	Calibrated Age (years B.P.) *	Calibrated Age (years before 2019) ***	Sample Description
Silver Fir	SilverFir-2	OS-163741	48.906001° N, -121.691409° W	175 ± 20	181± 44	N/A**	Outermost rings of a large old growth log wedged far into a ~1m thick exposure of well compacted muds and clays with angular, poorly sorted gravel and cobble sized rock fragments
	SilverFir-6	OS-163740	48.905903° N, -121.691956° W	2,020 ± 20	1959 ± 41	**2028**	Outermost rings of stratigraphically lowest, large old growth log protruding perpendicularly from deposit completely submerged in the Nooksack River
Bald Mountain	AM-log3	OS-163742	48.940782° N, -121.944287° W	125 ± 15	83 ± 62	N/A**	Sample from remains of stratigraphically lowest, moderately deteriorated, small log protruding perpendicularly from deposit.
	AM-log4	OS-163743	48.94072° N, -121.944218° W	3,350 ± 20	3593 ± 45	**3662**	Sample from remains of heavily deteriorated log encased in well compacted clays of exposed landslide toe.
Canyon Creek	SGLR-6	OS-163738	48.956167° N, -121.924196° W	39,300 ± 1,600	43899 ± 2650	N/A**	Sample from remains of moderately to heavily deteriorated log protruding from basal layer of deposit.
	SGLR-10	OS-163739	48.956051° N, -121.924258° W	41,600 ± 2,200	47124 ± 4925	N/A**	Sample from burnt wood fragment lodged in upper layer of deposit

*Calibrated age (years B.P.) refers to years before 1950 written as the median ± 2 standard deviations.
**N/A implies we did not use this sample for our age-roughness model
*** Age used in age-roughness model

4.2 Pacific Northwest Bedrock Landslide Age-Roughness Model

By fitting an exponential decay function to the eight landslides described above, there was a weak statistically significant correlation between age and deposit surface roughness ($r^2 = 0.45$, $p = 0.04$), likely due to the small sample size and relatively small range of ages (figure 6A). However, we note that the mean roughness values of bedrock landslides in the WCR exhibit similar mean roughness values to those in the OCR (LaHusen et al., 2020) (table 3 & table S1). This is expected as the source areas for landslides in the WCR and OCR have comparable lithologies. Roughness values from the OCR fall between 0.00861 m^{-1} for the oldest landslide at 40,900 ± 1,000 y.b.2019 and 0.0379 m^{-1} for the youngest landslide at 7 ± 1 y.b.2019. In our data, the landslide with the highest mean roughness value is the Bonneville landslide, with a roughness of 0.0190 m^{-1} and an age of 573 y.b.2019. The Damnation Creek landslide, our oldest landslide with an age of 7,908 y.b.2019 has the lowest mean roughness value at 0.0143 m^{-1}. We therefore decided to combine and fit the age-roughness data from both studies to create a Pacific Northwest bedrock landslide age-roughness model (figure 6A). When combined, landslide age and deposit surface roughness data display a more robust statistically significant correlation (>95% confidence, p = 6.357e-07) when fit by an exponential decay function (figure 6A):

$$t=339067e^{-345.2R}, \quad (3)$$

where t is the estimated landslide age in years before 2019, and R is the average roughness, in units of m^{-1} (figure 6A). We use this function to assign ages to the undated landslides and develop a landslide chronology of all the mapped landslides in the study area.

Table 3. Mean roughness values for landslide deposits of known age in Washington's Cascade Range			
Landslide Name	**MEAN Roughness (1/m)**	**Age (Years before 1950)**	**Age (Years before 2019)**
Bonneville	0.0190	504	573
Day Lake	0.0154	1540	1609
Van Zandt	0.0152	1300	1369
Racehorse Creek	0.0163	4234	4303
Church Mountain	0.0154	2414	2483
Damnation Creek	0.0143	7839	7908
Silver Fir	0.0150	1959	2028
Bald Mountain	0.0148	3593	3662

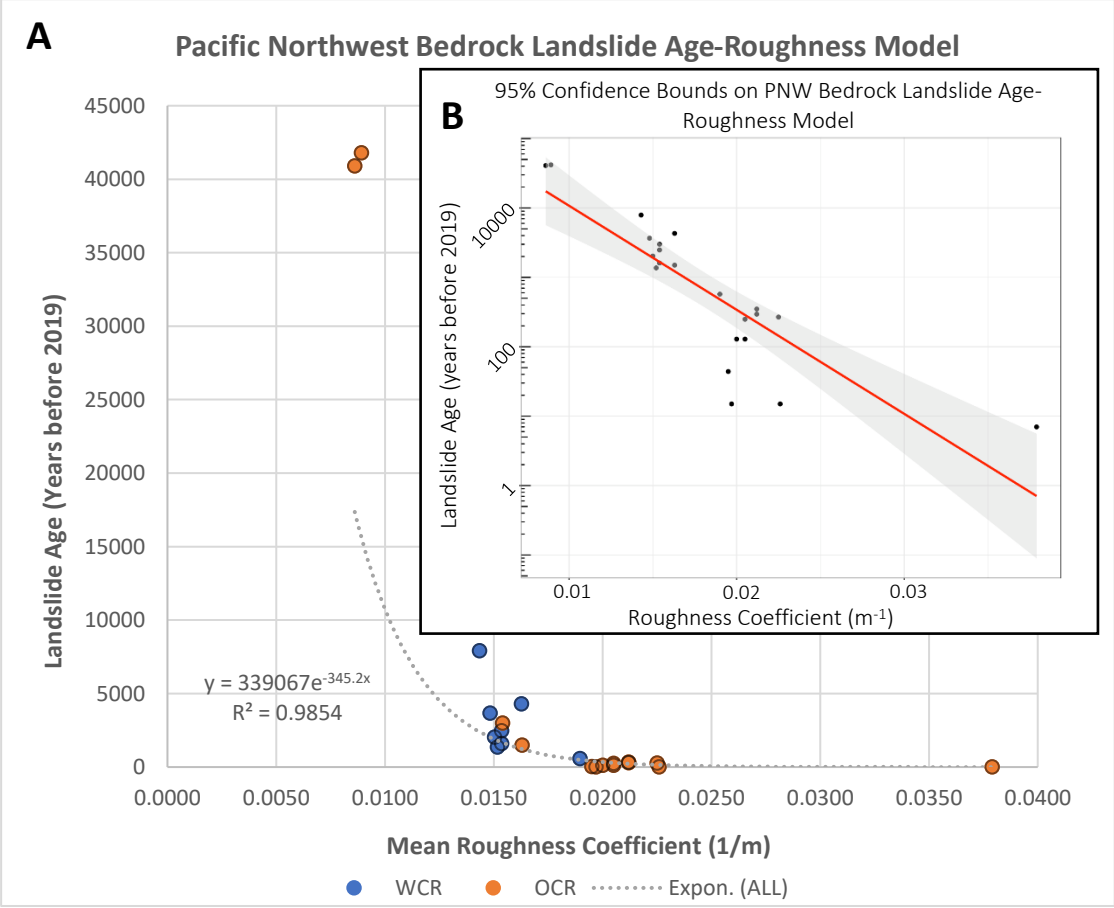

Figure 6. A) Pacific Northwest bedrock landslide age-roughness model. Blue data points indicate landslides in WCR, and orange data points indicate landslides in the OCR. **B)** Same data points and regression plotted on a semilog axis with 95% confidence intervals.

4.3 Western Whatcom County Landslide Chronology

Overall, the most obvious pattern in our landslide chronology for the region is the nonlinear decrease in landslide frequency with age through the Holocene (figure 7A). We relate this general trend to a preservation bias, which we expect as younger landslides display more readily identifiable morphologies on lidar derived slope and hillshade maps and as old slides reactivate (LaHusen et al., 2020). Discerning if and when landslide frequency differs from the background trend therefore is not plausible for times more than a few thousand years before present. However, zooming into a subset of more recent time better highlights undulations in landslide frequency. This reveals a broad peak in landslide frequency about 750-1250 years ago, as well as several peaks and troughs from about 2000-4000 years ago (figure 7B).

If the majority of the landslides occurring in the past 4000 years in our study are coseismic landslides, we would expect peaks in our landslide frequency history to track well with peaks in our modeled scenarios that incorporate landslide pulses at the time of ruptures on the BCF. Here, we see the simulated landslide history with coseismic landslide pulses most closely follows our observed landslide frequency history (figure 7B). Most noticeably, the peak around 1000 y.b.2019 in the earthquake model lines up with the observed peak, falling almost entirely within the 10^{th} and 90^{th} percentile bounds of the earthquake model. Landslide frequency also decreases from then to the present in both the simulation and data. In the earthquake model, 9.5% of the total landslides are caused by the youngest earthquake on the BCF, with 67 landslides occurring as a result.

Because our observed landslide frequency lines up well with that predicted by the earthquake model, we infer roughly 9.5% of landslides in our study area occurring in the past 4000 years were triggered by the youngest earthquake on the BCF. This observation is also supported by spatial clustering of large landslides with ages between 768 and 1234 y.b.2019 around and to the east of the BCF (figure 8A). For ages older than ~1250 y.b.2019, landslides in our observed data tend to better match the simulated landslide frequency history composed entirely of "background" landslides. This result is expected without a major event like an earthquake on the BCF. At around 3200 y.b.2019, the earthquake model displays a subdued peak in landslide frequency that is unmatched by our observed landslide frequency. Despite clear evidence for coseismic landslides with the youngest rupture on the BCF, there is no evidence for coseismic landsliding with the penultimate earthquake. Here, the irregular peaks and troughs where we might expect to see a pulse of coseismic landslides are likely a result of having low numbers of landslides of those ages due to preservation bias.

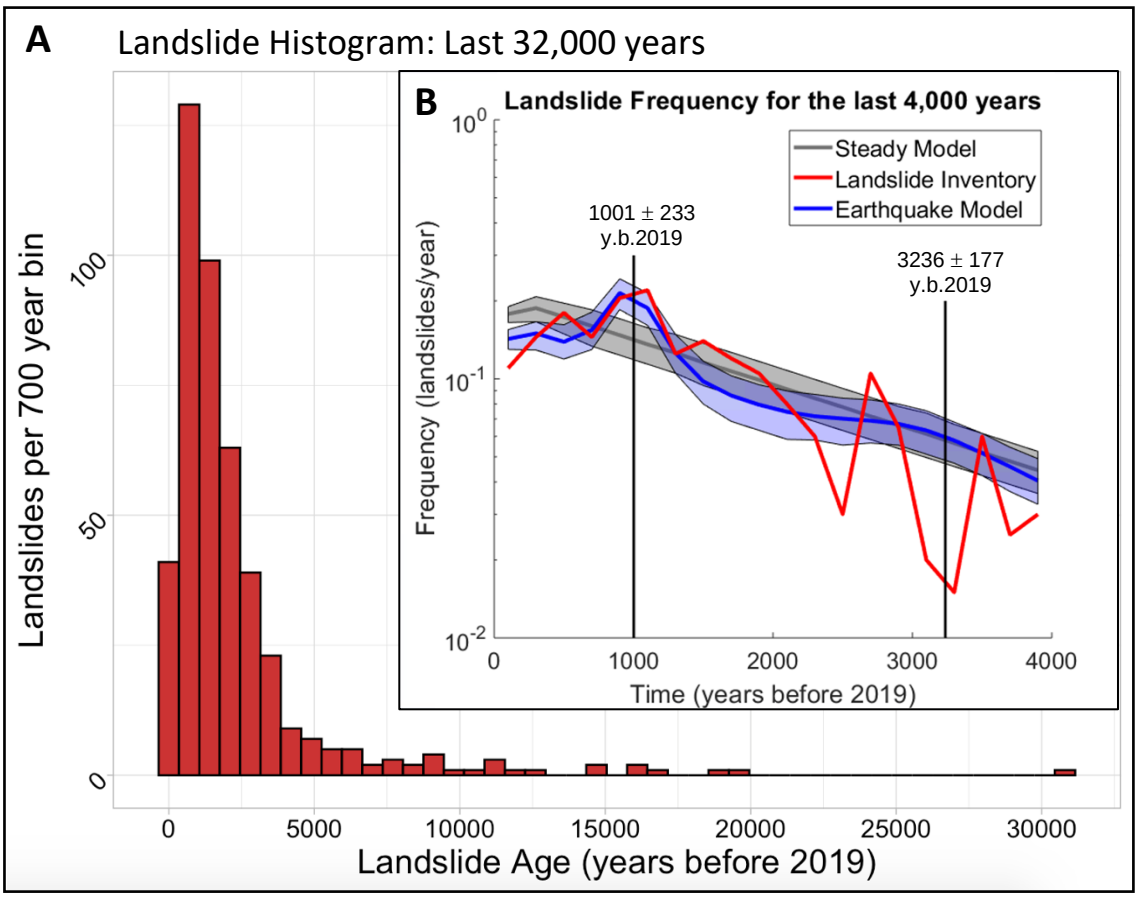

Figure 7. A) Histogram of landslide ages for the past 32,000 years across the study area. **B)** Comparison of observed versus simulated landslide frequency histories for the past 4000 years. Observed frequency calculated from age estimates for landslides mapped in the study area is plotted as a red line. Simulated landslide frequency for 10^4 modeled scenarios without earthquake pulses is shown in grey, Simulated landslide frequency for 10^4 modeled scenarios with earthquake pulses where 19% of all landslides occurred at the times of the two youngest ruptures on the Boulder Creek fault is shown in blue. Solid lines are the mean, and the shaded areas are the lower 10^{th} and upper 90^{th} percentiles of all model runs.

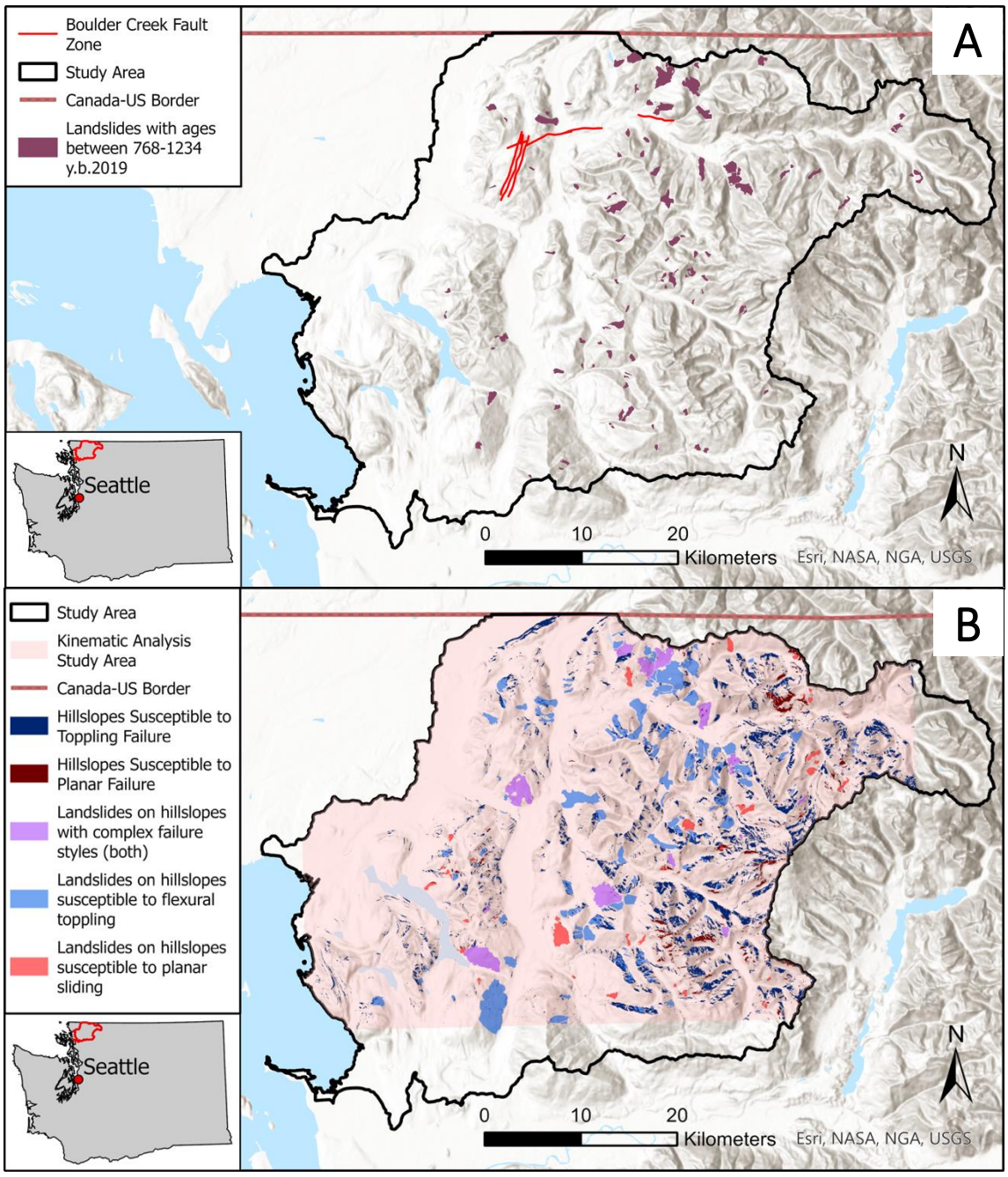

Figure 8. A) Location of 93 landslides with ages between 768-1234 y.b.2019. Landslides, especially the largest ones, represented as maroon polygons, appear to cluster around traces of the BCF, especially on the eastern side of the fault trace. Landslides become smaller and less frequent towards the south, and far eastern portion of the study area. **B) Areas susceptible to planar sliding and flexural toppling determined by our regional kinematic analysis.** Areas highlighted in dark red indicate hillslopes susceptible to planar sliding and areas highlighted in navy blue indicate slopes susceptible to toppling failures. Together, these areas make up ~6.6% of the region of analysis highlighted in light red. Landslides overlying these susceptible regions are represented by blue polygons (for flexural toppling), red polygons (for planar sliding), and purple polygons (complex failure style, i.e. overlying both types of susceptible regions).

4.4 Susceptibility to Planar Sliding and Flexural Toppling

Our regional kinematic analysis suggests the orientations of bedrock structures partly control landslide susceptibility. The areas susceptible to planar sliding or flexural toppling together make up ~6.6% of the analyzed region with 203 or 45.4% of landslides in our inventory overlying these susceptible regions (figure 8B). Of those, 150 landslides, or 33.6% of all landslides in our inventory, overlie hillslopes susceptible to flexural toppling while only 38, or 8.5% of all landslides, overlie hillslopes susceptible to planar sliding. In the southeastern and south-central portion of the study area, spatial patterns in landsliding appear to closely follow denoted areas susceptible to flexural toppling (figure 8B). An additional 15 landslides overlie hillslopes susceptible to both planar sliding and flexural toppling, which we deem complex failures. These 15 landslides generally have larger areas and are distributed throughout the study area. Furthermore, 40 of the total 203 landslides overlying susceptible regions also have ages consistent with the most recent earthquake (MRE) on the BCF (between 768 and 1234 y.b.2019), where three landslides in this age range occurred on slopes susceptible to both types of failure, six on slopes susceptible to planar sliding, and the remaining 31 on slopes susceptible to flexural toppling. Overall, bedrock structures may have predisposed slopes for failure and promoted more landslides over time than a single earthquake would throughout the study area.

5.0 Discussion

5.1 Hazard Implications

In this study, we demonstrated surface roughness of eight bedrock landslides in the WCR track well with age and are comparable to the surface roughness values of bedrock landslides in the OCR. We infer this correlation exists because the sedimentary rocks of the OCR are mechanically similar to those in our study area, such that they behave similarly in generating surface roughness when they fail as deep-seated landslides. Because of this, we combined the two datasets and derived the function that describes the best fit exponential regression to estimate the ages of 447 bedrock landslides in the Nooksack watershed, Washington. Similar to previous studies, the most predominant pattern in the resulting landslide chronology was a nonlinear decrease in frequency with age (Booth et al., 2017; LaHusen et al., 2020). However, a statistically unlikely deviation from this pattern around 1000 y.b.2019 was consistent with the simulated landslide frequency history that incorporates a pulse of 67 coseismic landslides at the times of the two most recent ruptures on the BCF. This consistency suggests 9.5% of all mapped bedrock landslides in the Nooksack Watershed in the past 4,000 years were triggered by the youngest earthquake on the BCF. It is likely, however, that this 9.5% is a minimum for landslides of all types, as our simulated landslide frequency histories, like our data, do not include smaller translational slides, or deep-seated landslides that are minimally displaced (head scarp < 2 m in height). Based on landslide frequency scaling relationships, these types of landslides, especially landslides smaller than our 93,000 m^2 threshold, may be expected to occur in far greater numbers than larger deep-seated, bedrock landslides (Keefer, 1984; Malamud et al., 2004a; Owen et al., 2008; Marc et al.,

2016). This implies that a greater number of total landslides may occur per earthquake event, that the model does not account for. Furthermore, the earthquake model incorporates a second pulse of 67 coseismic bedrock landslides at the time of the penultimate earthquake on the BCF (3236 y.b.2019) that is unmatched by our landslide frequency history. Because these 67 landslides are not reflected in our observed data around the time of the penultimate earthquake, they may have been reactivated in the younger earthquake. This further supports the likelihood that 9.5% of landslides occurring as a result of the MRE on the BCF is a minimum percentage. It is also possible these 67 landslides may be dispersed throughout the background of our observed data, such that the rate of background landsliding is higher than 0.16 landslides per year as the earthquake model suggests.

The spatial distribution of landslides with ages consistent with the MRE on the BCF are important to consider when thinking about hazard assessment. The United States Geological Survey (USGS) developed a ShakeMap for a scenario magnitude 6.8 earthquake on the BCF in which the most intense shaking is predicted to occur around Kendall Creek west of Maple Falls, WA (figure 9) (Washington Department of Natural Resources, 2012; United States Geological Survey, 2022). The intensity of shaking decreases radially with distance from the area immediately surrounding Kendall Creek, except in some of the nearby low-lying areas, such as the Nooksack River valley and the eastern half of the Puget Lowlands within Whatcom County (figure 9). The results of this modeled scenario however do not completely agree with the spatial distribution of landslides we determined to be consistent with the MRE on the BCF. Our results suggest distinct directionality, with far more particularly large landslides occurring on the steeper

slopes east of the BCF than in the bedrock slopes just west of the BCF (figure 8A). Based on the ShakeMap, areas predicted to experience very strong to extreme ground shaking in the case of a magnitude 6.8 earthquake on the BCF would likely incur moderate to very heavy damages. While this may hold true, our results suggest potential damage due to coseismic landsliding extends much further east than the ShakeMap suggests.

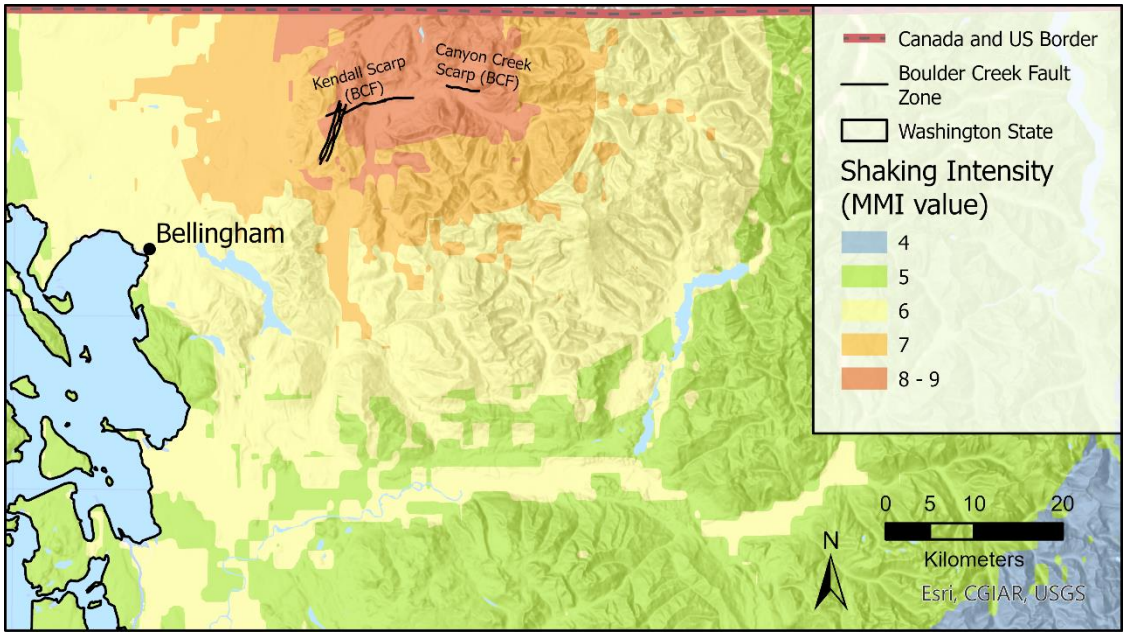

Figure 9. ShakeMap for a scenario magnitude 6.8 earthquake on the BCF developed by the USGS. Note the radial pattern of intense shaking surrounding the Kendall Creek and Canyon Creek scarps (United States Geological Survey, 2022).

With landslides being one of the greatest secondary hazards of earthquakes, it is important we continue to evolve our understanding of the complex relationship between coseismic landsliding and influencing factors (Keefer, 1984). Common influencing factors used in coseismic landslide susceptibility mapping include and are not limited to peak ground accelerations (PGA), geomorphometric features, and geologic features (Meunier et al., 2007; Owen et al., 2008; Shao and Xu, 2022). Our results reinforce the importance of considering PGA in addition to the surrounding geomorphometric features

and geologic features when assessing a region's susceptibility to coseismic landsliding. Of the 203 landslides we determined to be overlying hillslopes susceptible to planar sliding or flexural toppling, 40 have ages consistent with the MRE on the BCF. Notably, these 40 landslides constitute roughly two-thirds of the landslides that would occur in the event of an earthquake on the BCF as demonstrated by the earthquake model. This suggests structural orientations of bedrock are particularly important for understanding susceptibility to coseismic landsliding in the Nooksack watershed. Furthermore, more landslides with ages consistent with the MRE on the BCF occurred south or south-east of the fault, on the hanging wall. Although we didn't continue our mapping north of the U.S.-Canada border we suspect the apparent clustering on the hanging wall of the BCF is no coincidence as it has been observed in other coseismic landslide inventories (Owen et al., 2008; Chen et al., 2018; Shao and Xu, 2022). The results of this study point to the importance of considering more than just PGA associated with earthquakes when assessing for coseismic landslide susceptibility throughout a region.

5.2 Sources of Uncertainty

Because radiocarbon ages are the fundamental data needed to develop a landslide age-roughness relationship, we must acknowledge the uncertainty associated with radiocarbon dating. Obtaining the age of landslides is challenging due to the assumptions made when identifying sample sources that accurately reflect the true age of a landslide. We reduced the likelihood of large discrepancies between the sample source age and the true age of the landslide by following a set of criteria aimed at avoiding sampling sources not directly associated with the landslide event of interest, and by dating more than one sample per landslide. Having two dates per landslide allowed us to identify the sample

source age that most likely reflected the age of the landslide event of interest. Even after taking these necessary precautions, depending on whether the sample used to determine the age of the landslide was from a Douglas Fir tree, which can live up to at least 500 years, or a smaller Alder tree, which seldom live longer than 100 years, the difference between sampling the outer or inner growth rings of a log can result in tens to hundreds of years of uncertainty. However, compared to our newly acquired landslide ages of 1959 and 3593 cal. yrs B.P., this is uncertainty is still relatively small, on the order of ±10%. Aside from this contextual uncertainty, much of the error in radiocarbon dating stems from calibrating radiocarbon ages to calendar years (Scott et al., 2007). Calibrating radiocarbon ages requires a history of the amount of C^{14} in atmospheric CO_2, which has varied substantially in the last few centuries naturally, and due to anthropogenic emissions. The frequent peaks and troughs in the modern calibration curves limit the precision of our calibration, which is why our calibrated ages typically have about twice the uncertainty of the radiocarbon ages (table 2). Additionally, although the analytical uncertainty of the lab is much smaller that the latter sources of uncertainty, it is important to note that radiocarbon analyses run on the same sample under identical conditions would still produce slightly different results each time (Scott et al., 2007).

Despite the practical nature of the age-roughness model based on radiocarbon dates and used in this study, it does not come without error. Ideally, landslides with the same age would have the same roughness values, but natural variability in initial landslide roughness represents a source of uncertainty. A wide variety of sources such as slightly differing failure mechanisms, differing underlying lithology and structural orientations, and differing deposit geometries can all cause differences in initial

roughness conditions. We see this discrepancy in our analysis, where although the Day Lake and Church Mountain landslides have identical roughness values, based on the median age of the most likely calibrated age probability distribution, they failed ~874 years apart. In cases like these, the younger landslide (Day Lake landslide) deposit likely had a lower initial surface roughness than the older landslide (Church Mountain landslide), allowing time for erosional processes and soil diffusion to smooth the surface of the older, rougher landside deposit faster. Geomorphic transport laws and the exponential form of the age roughness regression itself support this observation (Roering et al., 1999; LaHusen et al., 2020).

Aside from natural variability in initial landslide deposit surface roughness, there are several sources of error in the roughness analysis itself. Calculating the roughness of a landslide deposit involves several steps, that may all introduce their own source of error. To start, we must have a compiled inventory of mapped landslide deposits. Landslide mapping is inherently subjective in nature, introducing human error to the analysis (Wills and McCrink, 2002). Here, the WA-DNR mapped most of the deposits dated by our age-roughness model, however, of the 392 DNR deposits in our inventory, we revised 54 and mapped an additional 55 for a total of 447 mapped landslide deposits. Despite following the same mapping protocol, one interpretation of a deposit boundary may differ from another, affecting the overall mean roughness of a deposit, biasing the age estimate one way or the other. The calculated roughness of the deposit can also be biased by the automatic removal of stream gullies and roads. Although we defined a drainage area threshold based on comparison to deposits with manually removed stream gully networks, removing stream gullies based on this threshold will inherently

overpredict the stream gully network for some deposits, and underpredict for others. For example, manual removal of stream gullies resulted in a larger total deposit area for the Bonneville landslide but a smaller total deposit area for the Day Lake landslide. These over and underpredictions suggest we chose a representative drainage area threshold, as it doesn't consistently over predict or underpredict the manually mapped stream gully network. Similarly, removing roads from all our mapped deposits using a road layer from WA-DNR provides an efficient alternative method to manually removing roads from every deposit. However, abandoned logging roads and private ways are not included in this dataset, consequently introducing higher roughness values along the roads' sharp edges, biasing the deposits roughness towards a higher value. Furthermore, we must consider the error associated with the lidar data used to compute roughness. Here, we use 0.9 m resolution DEMs, but natural variations in point densities throughout the point cloud used to create the DEM's can result in artifacts and differences in roughness (Berti et al., 2013). These areas appear as a mesh of triangulated facets and can result in lower roughness values due to their smooth interpolated appearance.

Considering these sources of uncertainty, we note this roughness dating technique is not meant for obtaining precise absolute ages of individual landslides within a specified region but is rather a more generalized landslide chronology tool that can be used to investigate broadscale spatial and temporal patterns in landsliding. Although the age estimates produced by our roughness model are less accurate than using traditional geochronology techniques such as radiocarbon dating or dendrochronology to date the 447 landslides in our study area, we show roughness dating is a powerful and practically

feasible tool for estimating the ages of several hundred landslides over broad swaths of land to better understand their driving mechanisms.

Similar to the age-roughness dating technique, our kinematic analysis provides a method to better understand what controls landslides, specifically how bedrock orientations may or may not control the spatial pattern of landsliding across a large region. This analysis is informative for looking at broadscale patterns, however, and may not be suitable for identifying the exact failure style of an individual landslide. Interpolation techniques heavily rely on dense data. With low data density, error is introduced into the interpolated result. In the case of our kinematic analysis, areas lacking attitude measurements may be assigned incorrect dip direction and dip angle values, which will then translate into our final susceptibility rasters. Furthermore, the 203 landslides underlain by slopes susceptible to planar sliding or flexural toppling were determined based on the criteria that they intersect with any of these susceptible regions. In some cases, landslide deposit polygons minimally intersect with cells in the determined susceptibility rasters in locations that may not accurately reflect the source area of a particular landslide, demonstrating bedrock orientation may not be the predominant reason for failure for all 203 landslides. Moreover, the 40 landslides that have ages consistent with the MRE on the BCF and also overlie slopes determined to be susceptible to planar sliding, flexural toppling, or both, may have existed as threshold slopes prior to the EQ event, and then failed at the time of rupture.

6.0 Conclusion

Determining the primary driving mechanisms of landslides within a region requires knowledge of the landslide chronology, yet dating landslides using traditional radiocarbon and dendrochronology techniques is not feasible at the regional scale. The lidar based surface roughness analysis preformed in this study provides means to overcome this barrier, allowing for regional scale investigations of landslide driving mechanisms. This is especially important in regions like Washington state, where long duration and/or high intensity rainfall, landslide conducive geology, and regional tectonics are all likely landslide triggers. Using a continuous wavelet transform with a 20 m Mexican hat wavelet, we quantified deposit surface roughness of eight landslides of known age in Washington's Cascade Range and combined those ages with data from the Oregon Coast Range to derive a Pacific Northwest bedrock landslide age-roughness model. We used this model to predict the age of 447 mapped bedrock landslides in the Nooksack Watershed, western Whatcom County, Washington. Landslide frequency broadly decreased nonlinearly with age, which we linked to a preservation bias. However, deviations from that overall trend were consistent with a simulated landslide frequency that incorporates coseismic landslide pulses at the times of known ruptures on the Boulder Creek fault in the past 4,000 years. This suggested roughly 9.5% of the landslides in our study area in the past 4,000 years were coseismic with the most recent earthquake on the Boulder Creek fault about 1,000 years before 2019. This was further supported by visually apparent spatial clustering of larger landslide deposits with ages between 768 and 1,234 years before 2019 near the trace of the Boulder Creek fault. Other spatial patterns in landsliding appeared to mainly reflect hillslopes where flexural

toppling is kinematically feasible. Our results suggest earthquakes and bedrock orientations, specifically those conducive to flexural toppling, influenced the spatial distribution of landslides throughout the Nooksack watershed, while an earthquake about 1,000 years before 2019 also made a detectable mark on the temporal pattern.

These results are important for hazard assessment and planning, as they suggest a surface rupturing earthquake on the Boulder Creek fault will cause roughly 67 additional large, deep-seated bedrock landslides throughout the region. In addition to being hazardous themselves, these landslides have the potential to inundate rivers creating temporary dams that could eventually breach, resulting in catastrophic outburst floods. The associated floodwaters could rapidly flow towards Bellingham or smaller towns in the Nooksack watershed, resulting in extensive property and economic damage.

Our findings suggest the evolution of the Nooksack watershed is dominated by non-seismic landslides with occasional pulses of coseismic landslides. We can expect erosion rates to exceed the long-term average rates caused by tectonic uplift, especially after earthquakes on the Boulder Creek fault.

References

Barnett, E.A., 2007, Active faulting at the Northeast margin of the greater Puget Lowland: A paleoseismic and magnetic-anomaly study of the Kendall fault scarp, Whatcom County, Northwest Washington: Humboldt State University.

Berti, M., Corsini, A., and Daehne, A., 2013, Comparative analysis of surface roughness algorithms for the identification of active landslides: Geomorphology, v. 182, p. 1–18, doi:https://doi.org/10.1016/j.geomorph.2012.10.022.

Bilderback, E.L., Pettinga, J.R., Litchfield, N.J., Quigley, M., Marden, M., Roering, J.J., and Palmer, A.S., 2014, Hillslope response to climate-modulated river incision in the Waipaoa catchment, east coast North Island, New Zealand: Geological Society of America bulletin, v. 127, p. 131–148.

Bird, J.F., and Bommer, J.J., 2004, Earthquake losses due to ground failure: Engineering Geology, v. 75, p. 147–179, doi:https://doi.org/10.1016/j.enggeo.2004.05.006.

Blodgett, T.A., and Isacks, B.L., 2007, Landslide Erosion Rate in the Eastern Cordillera of Northern Bolivia: Earth Interactions, v. 11, p. 1- n/a, doi:10.1175/2007EI222.1.

Booth, A., Dehls, J., Eiken, T., Fischer, L., Hermanns, R., and Oppikofer, T., 2014, Integrating diverse geologic and geodetic observations to determine failure mechanisms and deformation rates across a large bedrock landslide complex: the Osmundneset landslide, Sogn og Fjordane, Norway: Landslides, v. 12, doi:10.1007/s10346-014-0504-y.

Booth, A.M., LaHusen, S.R., Duvall, A.R., and Montgomery, D.R., 2017, Holocene history of deep-seated landsliding in the North Fork Stillaguamish River valley from surface roughness analysis, radiocarbon dating, and numerical landscape evolution modeling: Journal of Geophysical Research: Earth Surface, v. 122, p. 456–472, doi:https://doi.org/10.1002/2016JF003934.

Booth, A., Roering, J., and Perron, J., 2009, Automated landslide mapping using spectral analysis and high-resolution topographic data: Puget Sound lowlands, Washington, and Portland Hills, Oregon: Geomorphology, v. 109, p. 132–147.

Booth, A.M., Roering, J.J., and Rempel, A.W., 2013, Topographic signatures and a general transport law for deep-seated landslides in a landscape evolution model: Journal of Geophysical Research: Earth Surface, v. 118, p. 603–624, doi:10.1002/jgrf.20051.

Booth, D., Troost, K., and Clague, J., 2003, The Cordilleran Ice Sheet: The Quaternary Period in the United States,.

Brideau, M.-A., Stead, D., Kinakin, D., and Fecova, K., 2005, Influence of tectonic structures on the Hope Slide, British Columbia, Canada: Engineering Geology, v. 80, p. 242–259, doi:10.1016/j.enggeo.2005.05.004.

Bronk Ramsey, C., 2009, Bayesian Analysis of Radiocarbon Dates: Radiocarbon, v. 51, p. 337–360, doi:10.1017/S0033822200033865.

Brunengo, M.J., 2001, The Van Zandt Dike Landslide and a Medley of Other Mass-Movement Features in the Samish - South Nooksack Trough: Northwest Geological Society Society Field Trips in Pacific Northwest Geology.

Caine, N., 1980, The Rainfall Intensity - Duration Control of Shallow Landslides and Debris Flows: Geografiska annaler. Series A, Physical geography, v. 62, p. 23–27.

Chen, X., Liu, C., Wang, M., and Zhou, Q., 2018, Causes of unusual distribution of coseismic landslides triggered by the Mw 6.1 2014 Ludian, Yunnan, China earthquake: Journal of Asian Earth Sciences, v. 159, p. 17–23, doi:10.1016/j.jseaes.2018.03.010.

Collins, B.D., and Reid, M.E., 2019, Enhanced landslide mobility by basal liquefaction: The 2014 State Route 530 (Oso), Washington, landslide: GSA Bulletin, v. 132, p. 451–476, doi:10.1130/B35146.1.

Crider, J.G., Tucker, D.S., Clark, D.H., and Linneman, S.R., 2009, The 2009 Racehorse Creek Landslide: Forensic dynamics of a large, complex catastrophic mass movement: Geological Society of America Abstracts with Programs, v. 41, p. 498.

Fan, X., Dufresne, A., Subramanian, S.S., Strom, A., Hermanns, R., Stefanelli, C.T., Hewitt, K., Yunus, A.P., Dunning, S., Capra, L. and Geertsema, M., 2020. The formation and impact of landslide dams–State of the art. *Earth-Science Reviews*, *203*, p.103116.

Ganerød, G.V., Grøneng, G., Rønning, J.S., Dalsegg, E., Elvebakk, H., Tønnesen, J.F., Kveldsvik, V., Eiken, T., Blikra, L.H., and Braathen, A., 2008, Geological model of the Åknes rockslide, western Norway: Engineering Geology, v. 102, p. 1–18, doi:10.1016/j.enggeo.2008.01.018.

Gischig, V., Preisig, G., and Eberhardt, E., 2015, Numerical Investigation of Seismically Induced Rock Mass Fatigue as a Mechanism Contributing to the Progressive Failure of Deep-Seated Landslides: Rock Mechanics and Rock Engineering, v. 49, doi:10.1007/s00603-015-0821-z.

Glenn, N.F., Streutker, D.R., Chadwick, D.J., Thackray, G.D., and Dorsch, S.J., 2006, Analysis of LiDAR-derived topographic information for characterizing and

differentiating landslide morphology and activity: Geomorphology, v. 73, p. 131–148, doi:https://doi.org/10.1016/j.geomorph.2005.07.006.

Goetz, J., Bell, R., and Brenning, A., 2014, Could surface roughness be a poor proxy for landslide age? Results from the Swabian Alb, Germany: Earth Surface Processes and Landforms, v. 39, doi:10.1002/esp.3630.

Guglielmi, Y., Cappa, F., and Binet, S., 2005, Coupling between hydrogeology and deformation of mountainous rock slopes: Insights from La Clapière area (southern Alps, France): Comptes Rendus Geoscience, v. 337, p. 1154–1163, doi:10.1016/j.crte.2005.04.016.

Hermanns, R.L., and Strecker, M.R., 1999, Structural and lithological controls on large Quaternary rock avalanches (sturzstroms) in arid northwestern Argentina: GSA Bulletin, v. 111, p. 934–948, doi:10.1130/0016-7606(1999)111<0934:SALCOL>2.3.CO;2.

Hovius, N., Stark, C.P., and Allen, P.A., 1997, Sediment flux from a mountain belt derived by landslide mapping: Geology, v. 25, p. 231–234, doi:10.1130/0091-7613(1997)025<0231:SFFAMB>2.3.CO;2.

Iverson, R.M. et al., 2015, Landslide mobility and hazards: implications of the 2014 Oso disaster: Earth and Planetary Science Letters, v. 412, p. 197–208, doi:10.1016/j.epsl.2014.12.020.

Jacoby, G.C., Williams, P.L., and Buckley, B.M., 1992, Tree Ring Correlation Between Prehistoric Landslides and Abrupt Tectonic Events in Seattle, Washington: Science (American Association for the Advancement of Science), v. 258, p. 1621–1623.

Jomard, H., Lebourg, T., Guglielmi, Y., and Tric, E., 2010, Electrical imaging of sliding geometry and fluids associated with a deep seated landslide (La Clapière, France): Earth Surface Processes and Landforms, v. 35, p. 588–599, doi:10.1002/esp.1941.

Keaton, J.R., and DeGraff, J.V., 1996, Surface Observation and Geologic Mapping, *in* Landslides: Investigation and Mitigation, Transportation Research Board, Special Report 247.

Keefer, D.K., 1984, Landslides caused by earthquakes: Geological Society of America bulletin, v. 95, p. 406.

Kelsey, H.M., 1978, Earthflows in Franciscan melange, Van Duzen River basin, California: Geology, v. 6, p. 361–364, doi:10.1130/0091-7613(1978)6<361:EIFMVD>2.0.CO;2.

Kelsey, H.M., Sherrod, B.L., Blakely, R.J., and Haugerud, R.A., 2012, Holocene faulting in the Bellingham forearc basin: Upper-plate deformation at the northern end of the Cascadia subduction zone: Journal of Geophysical Research: Solid Earth, v. 117, p. n/a.

LaHusen, S.R., Duvall, A.R., Booth, A.M., Grant, A., Mishkin, B.A., Montgomery, D.R., Struble, W., Roering, J.J., and Wartman, J., 2020, Rainfall triggers more deep-seated landslides than Cascadia earthquakes in the Oregon Coast Range, USA: Science advances, v. 6, p. eaba6790.

LaHusen, S.R., Duvall, A.R., Booth, A.M., and Montgomery, D.R., 2016, Surface roughness dating of long-runout landslides near Oso, Washington (USA), reveals persistent postglacial hillslope instability: Geology, v. 44, p. 111–114, doi:10.1130/G37267.1.

Lapen, T.J., 2000, Geologic Map of the Bellingham 1:100,000 Quadrangle, Washington: Open File Report 2000–5.

Larsen, I.J., and Montgomery, D.R., 2012, Landslide erosion coupled to tectonics and river incision: Nature Geoscience, v. 5, p. 468–473, doi:10.1038/ngeo1479.

Lashermes, B., Foufoula-Georgiou, E., and Dietrich, W.E., 2007, Channel network extraction from high resolution topography using wavelets: Geophysical Research Letters, v. 34, doi:10.1029/2007GL031140.

Malamud, B.D., Turcotte, D.L., Guzzetti, F., and Reichenbach, P., 2004a, Landslide inventories and their statistical properties: Earth Surface Processes and Landforms, v. 29, p. 687–711, doi:https://doi.org/10.1002/esp.1064.

Malamud, B.D., Turcotte, D.L., Guzzetti, F., and Reichenbach, P., 2004b, Landslides, earthquakes, and erosion: Earth and Planetary Science Letters, v. 229, p. 45–59, doi:10.1016/j.epsl.2004.10.018.

Malick, G., 2018, Geologic Development and Ongoing Activity of the Van Zandt Landslide Complex, Northwest WA, USA: Western Washington University, https://cedar.wwu.edu/wwuet/637/.

Marc, O., Hovius, N., Meunier, P., Gorum, T., and Uchida, T., 2016, A seismologically-consistent expression for the total area and volume of earthquake-triggered landsliding: Journal of Geophysical Research: Earth Surface, v. 121, doi:10.1002/2015JF003732.

McKean, J., and Roering, J., 2004, Objective landslide detection and surface morphology mapping using high-resolution airborne laser altimetry: Geomorphology, v. 57, p. 331–351, doi:10.1016/S0169-555X(03)00164-8.

Meunier, P., Hovius, N., and Haines, A.J., 2007, Regional patterns of earthquake-triggered landslides and their relation to ground motion: Geophysical Research Letters, v. 34, p. L20408, doi:10.1029/2007GL031337.

Mickelson, K.A., Contreras, T.A., Gallin, W.N., Jacobacci, K.E., and Slaughter, S.L., 2020, Landslide inventory of western Whatcom County, Washington: Washington Geological Survey Report of Investigations 42 42.

Norrish, N.I., and Wyllie, D.C., 1996, Landslides: Investigation and Mitigation: Chapter 15 - Rock slope stability analysis. Transportation Research Board Special Report 247.

Owen, L.A., Kamp, U., Khattak, G.A., Harp, E.L., Keefer, D.K., and Bauer, M.A., 2008, Landslides triggered by the 8 October 2005 Kashmir earthquake: Geomorphology, v. 94, p. 1–9, doi:10.1016/j.geomorph.2007.04.007.

Pánek, T., 2014, Recent progress in landslide dating: A global overview: Progress in Physical Geography, v. 39, p. 168–198, doi:10.1177/0309133314550671.

Parker, R.N., Densmore, A.L., Rosser, N.J., de Michele, M., Li, Y., Huang, R., Whadcoat, S., and Petley, D.N., 2011, Mass wasting triggered by the 2008 Wenchuan earthquake is greater than orogenic growth: Nature Geoscience, v. 4, p. 449–452, doi:10.1038/ngeo1154.

Pringle, P., 2009, The Bonneville Slide: Explorations: Columbia Gorge Interpretive Center Museum, p. 2–3.

Pringle, P.T., Reynolds, N.D., O'Connor, J.E., Schuster, R.L., Weaver, R., and Black, B., 2021, Tree-Ring Dating of the Bonneville Landslide to Late 1446 or Early 1447 CE: Geological Society of America Abstracts with Programs, v. 53, doi:10.1130/abs/2021AM-369596.

Pringle, P.T., Schuster, R.L., and Logan, R.L., 1998, New Radiocarbon Ages of Major Landslides in the Cascade Range, Washington, *in* Washington Geology, Olympia, WA, Washington Dept. of Natural Resources, Division of Geology and Earth Resources, v. 26, p. 31–39.

Reynolds, N., O'Connor, J., Pringle, P., Schuster, R.L., and Bourdeau, A., 2015, Age of the Bonneville landslide and the drowned forest of the Columbia River, Washington, USA—From wiggle-match radiocarbon dating and tree ring analysis [abstract]:

Roering, J.J., Kirchner, J.W., and Dietrich, W.E., 2005, Characterizing structural and lithologic controls on deep-seated landsliding; implications for topographic relief and landscape evolution in the Oregon Coast Range, USA: Geological Society of America bulletin, v. 117, p. 654–668.

Roering, J., Kirchner, J., and Dietrich, W., 1999, Evidence for nonlinear, diffusive sediment transport on hillslopes and implications for landscape morphology: Water Resources Research, v. 35, p. 853–870, doi:10.1029/1998WR900090.

Schmidt, K.M., and Montgomery, D.R., 1995, Limits to relief: Science, v. 270, p. 617.

Schulz, W.H., 2007, Landslide susceptibility revealed by LIDAR imagery and historical records, Seattle, Washington: Engineering Geology, v. 89, p. 67–87, doi:10.1016/j.enggeo.2006.09.019.

Scott, E.M., Cook, G.T., and Naysmith, P., 2007, Error and Uncertainty in Radiocarbon Measurements: Radiocarbon, v. 49, p. 427–440, doi:10.1017/S0033822200042351.

Shao, X., and Xu, C., 2022, Earthquake-induced landslides susceptibility assessment: A review of the state-of-the-art: Natural Hazards Research, v. 2, p. 172–182, doi:https://doi.org/10.1016/j.nhres.2022.03.002.

Sherrod, B.L., Barnett, E., Schermer, E.R., Kelsey, H., Hughes, J.F., Foit, F.F., Weaver, C.S., Haugerud, R.A., and Hyatt, T.L., 2013, Holocene tectonics and fault reactivation in the foothills of the north Cascade Mountains, Washington: Geosphere, v. 9, p. 827–852.

Sherrod, B., and Gomberg, J., 2014, Crustal earthquake triggering by pre-historic great earthquakes on subduction zone thrusts: Journal of Geophysical Research: Solid Earth, v. 119, p. 1273–1294, doi:https://doi.org/10.1002/2013JB010635.

Slaughter, S.L., Burns, W.J., Mickelson, K.A., Jacobacci, K.E., Biel, A., and Contreras, T.A., 2017, Protocol for Landslide Inventory Mapping form Lidar Data in Washington State: Washington Geological Survey Bulletin 82 82.

Stark, T.D., Baghdady, A.K., Hungr, O., and Aaron, J., 2017, Case Study: Oso, Washington, Landslide of March 22, 2014—Material Properties and Failure Mechanism: Journal of Geotechnical and Geoenvironmental Engineering, v. 143, p. 05017001, doi:10.1061/(ASCE)GT.1943-5606.0001615.

Tabor, R.W., Haugerud, R.A., Hildreth, W., and Brown, E.H., 2003, Geologic map of the Mount Baker 30- by 60-Minute Quadrangle: Geologic Investigations Series I–2660.

Torrence, C., and Compo, G.P., 1998, A Practical Guide to Wavelet Analysis: Bulletin of the American Meteorological Society, v. 79, p. 61–78.

United States Geological Survey, 2022, Earthquake Scenarios:, https://www.usgs.gov/tools/earthquake-scenarios.

Wartman, J., Montgomery, D.R., Anderson, S.A., Keaton, J.R., Benoît, J., dela Chapelle, J., and Gilbert, R., 2016, The 22 March 2014 Oso landslide, Washington, USA: Geomorphology, v. 253, p. 275–288, doi:10.1016/j.geomorph.2015.10.022.

Washington Department of Natural Resources, 2012, Understanding Earthquake Hazards in Washington State: Modeling a Magnitude 6.8 Earthquake on the Boulder Creek Fault Zone in Whatcom County: Scenario Earthquakes for Washington State, https://www.dnr.wa.gov/Publications/ger_seismic_scenario_boulder_creek.pdf.

Washington Department of Natural Resources, 2022, Washington Department of Natural Resources State Lands - Roads: Roads Feature Class.

Wells, R.E., and Simpson, R.W., 2001, Northward migration of the Cascadia forearc in the northwestern U.S. and implications for subduction deformation: Earth, planets, and space, v. 53, p. 275–283.

Wills, C.J., and McCrink, T.P., 2002, Comparing landslide inventories: The map depends on the method: Environmental & Engineering Geoscience, v. 8, p. 279–293, doi:10.2113/8.4.279.

Appendix A. The Oso Landslide

Figure S1. Photo of the Oso landslide taken 42 days after the hillslope failed on March 22, 2014. Figure adopted from Wartman et al., 2016. Although a landslide in glacial sediments, rather than bedrock, this landslide is similar in volume and area to landslides used in our study.

Appendix B. The Deforming Cascadia Forearc

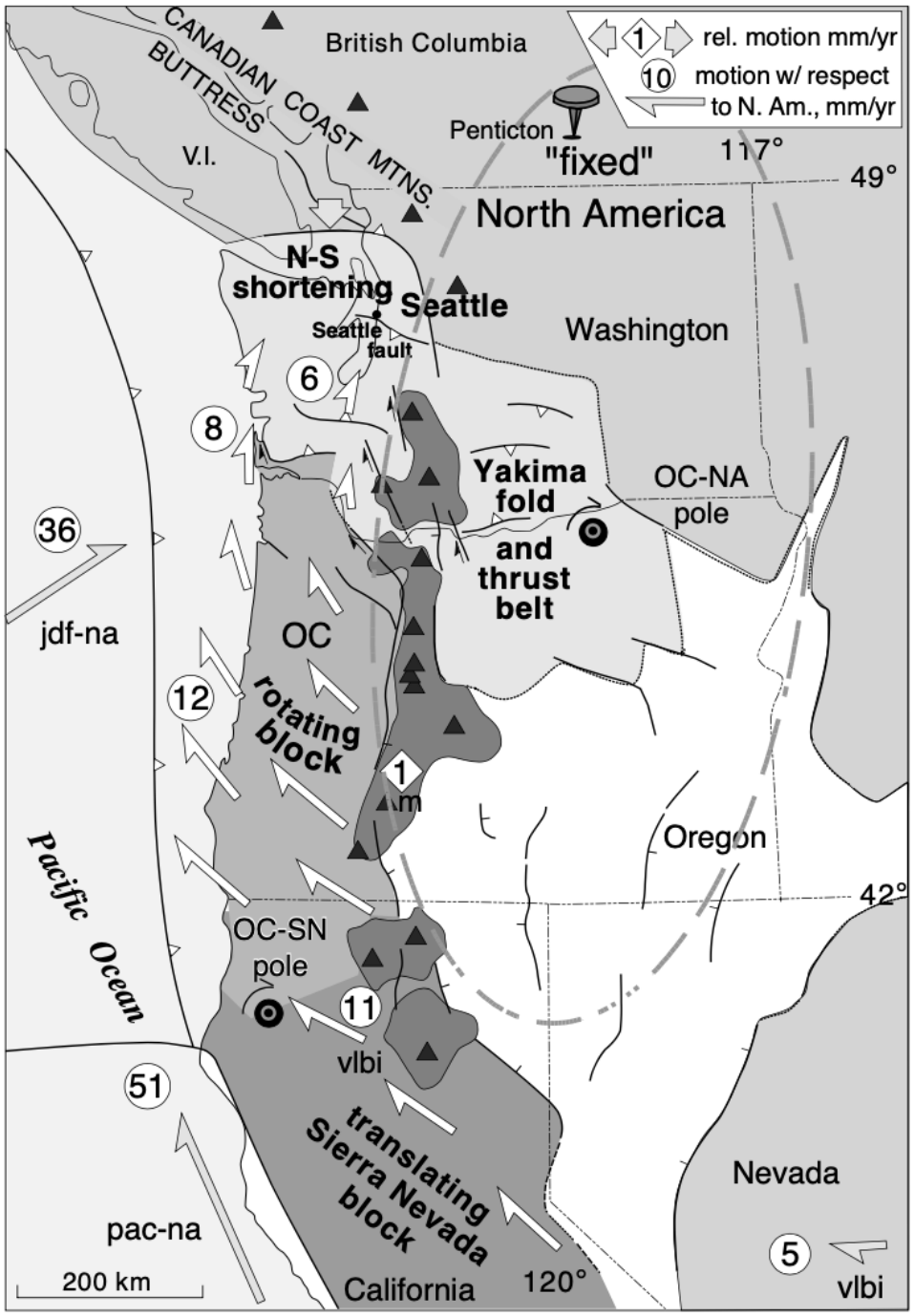

Figure S2. Revised microplate model showing the overall clockwise motion of the Cascadia forearc. Figure from Wells and Simpson, 2001. The area of focus in this study is the region labeled N-S shortening, immediately south of the Canadian Coast Mountains buttress. As a result. this region hosts several Holocene active crustal faults, including the Boulder Creek Fault.

Appendix C. Field Work – Sampling:

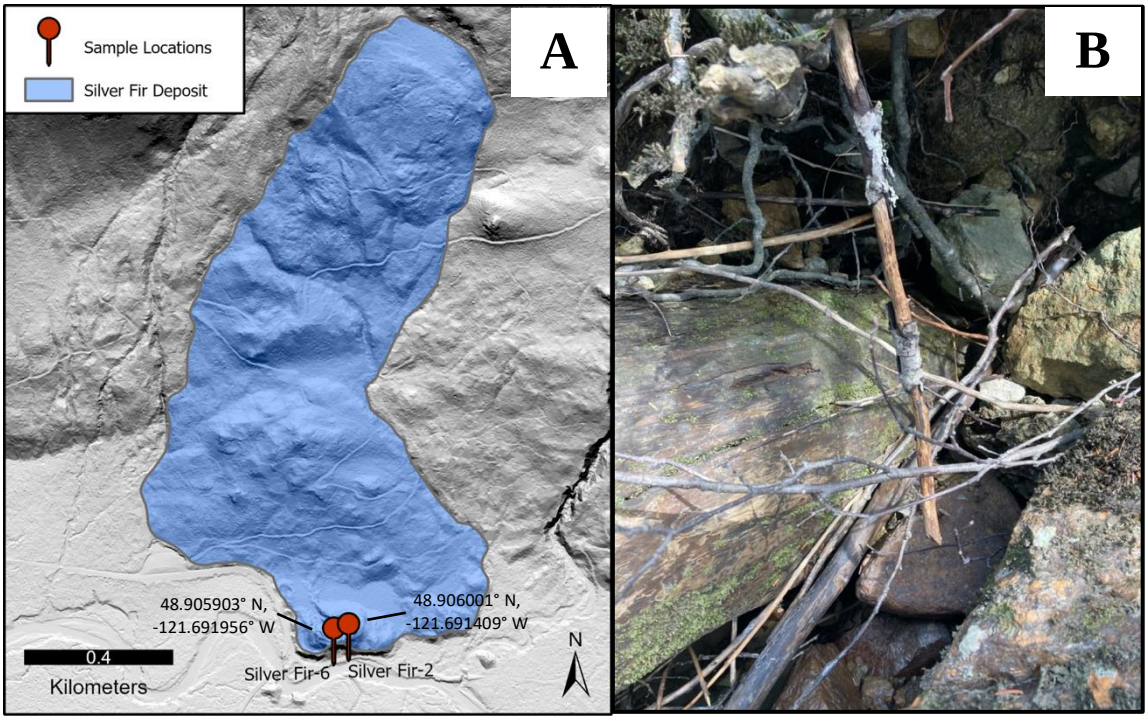

Figure S3. A) Blue deposit polygon for the Silver Fir landslide draped over a hillshade map derived from ~0.9m bare earth lidar imagery obtained from WA-DNR's lidar portal. Sample locations are denoted as red pins with the corresponding sample name and GPS coordinates labeled accordingly. **B)** Large old growth log with a ~50 cm diameter protruding out from far back within the landslide deposit where we obtained sample "SilverFir-2" from. Note, for this landslide we could not take a clear picture of the log we obtained sample "SilverFir-6" from, as it was completely submerged in the Nooksack River.

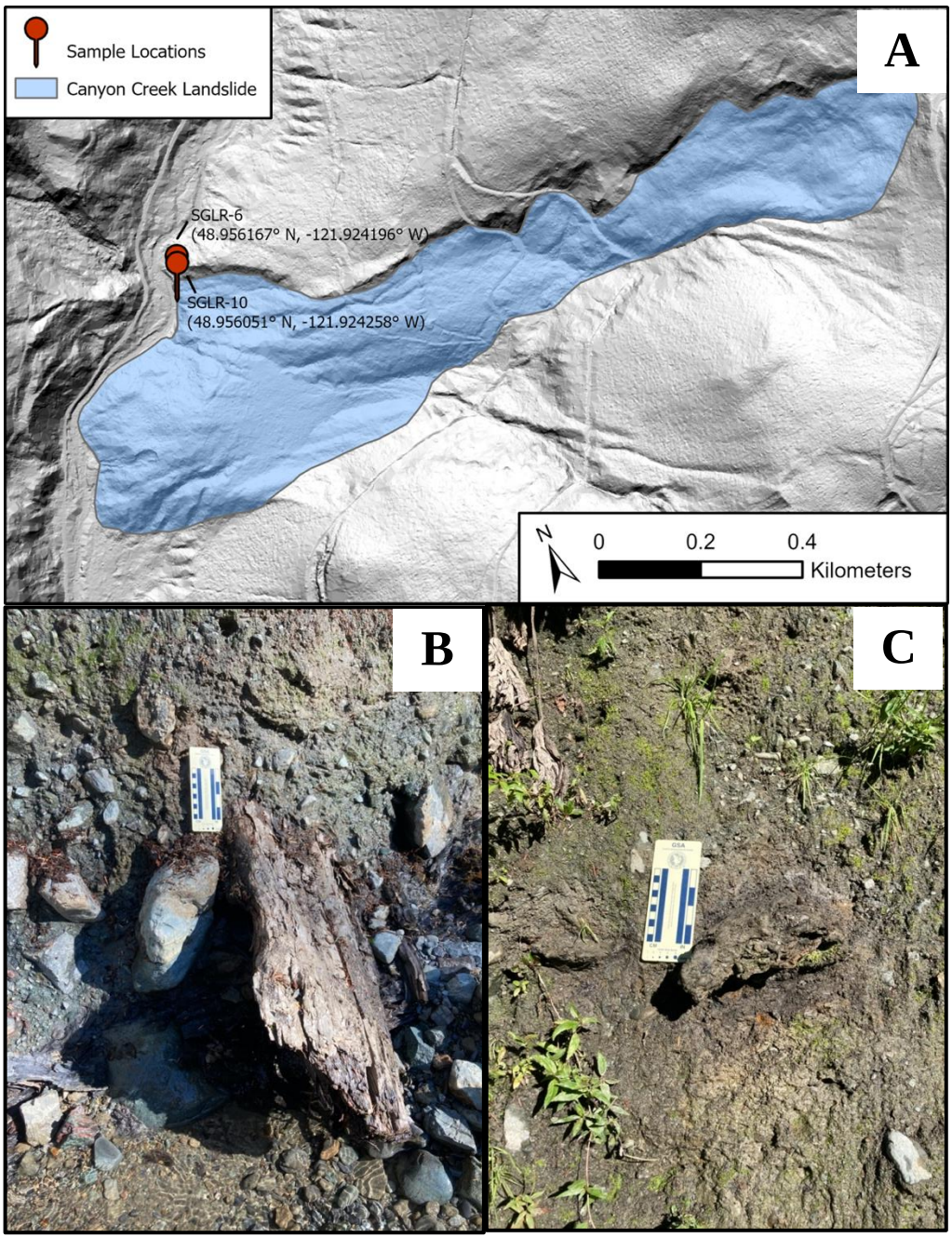

Figure S4. A) Blue deposit polygon for the Canyon Creek landslide draped over a hillshade map derived from ~0.9m bare earth lidar imagery obtained from WA-DNR's lidar portal. Sample locations are denoted as red pins with the corresponding sample name and GPS coordinates labeled accordingly. **B)** Moderately deteriorated log protruding from basal layer of deposit where we collected sample SGLR-6. **C)** Burnt wood fragment in upper layer of deposit where we collected sample SGLR-10. Note the difference in color between the surrounding clays in the basal and upper layers of the deposit. GSA scales are 10 cm.

Appendix D. Two-Dimensional Mexican hat wavelet

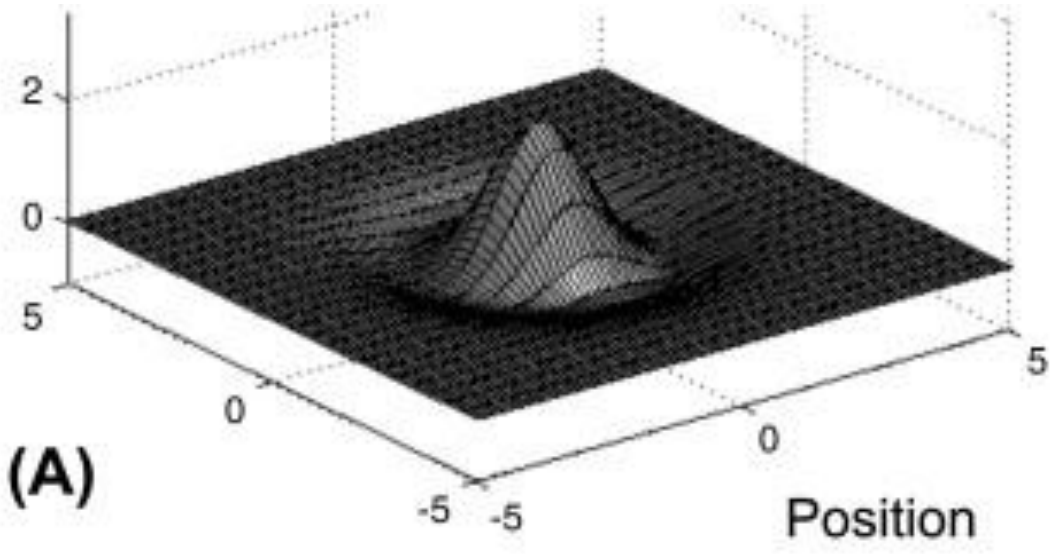

Figure S5. Figure from Booth et al. (2009) displaying a two-dimensional Mexican hat wavelet.

Appendix E. Landslide Failure Styles

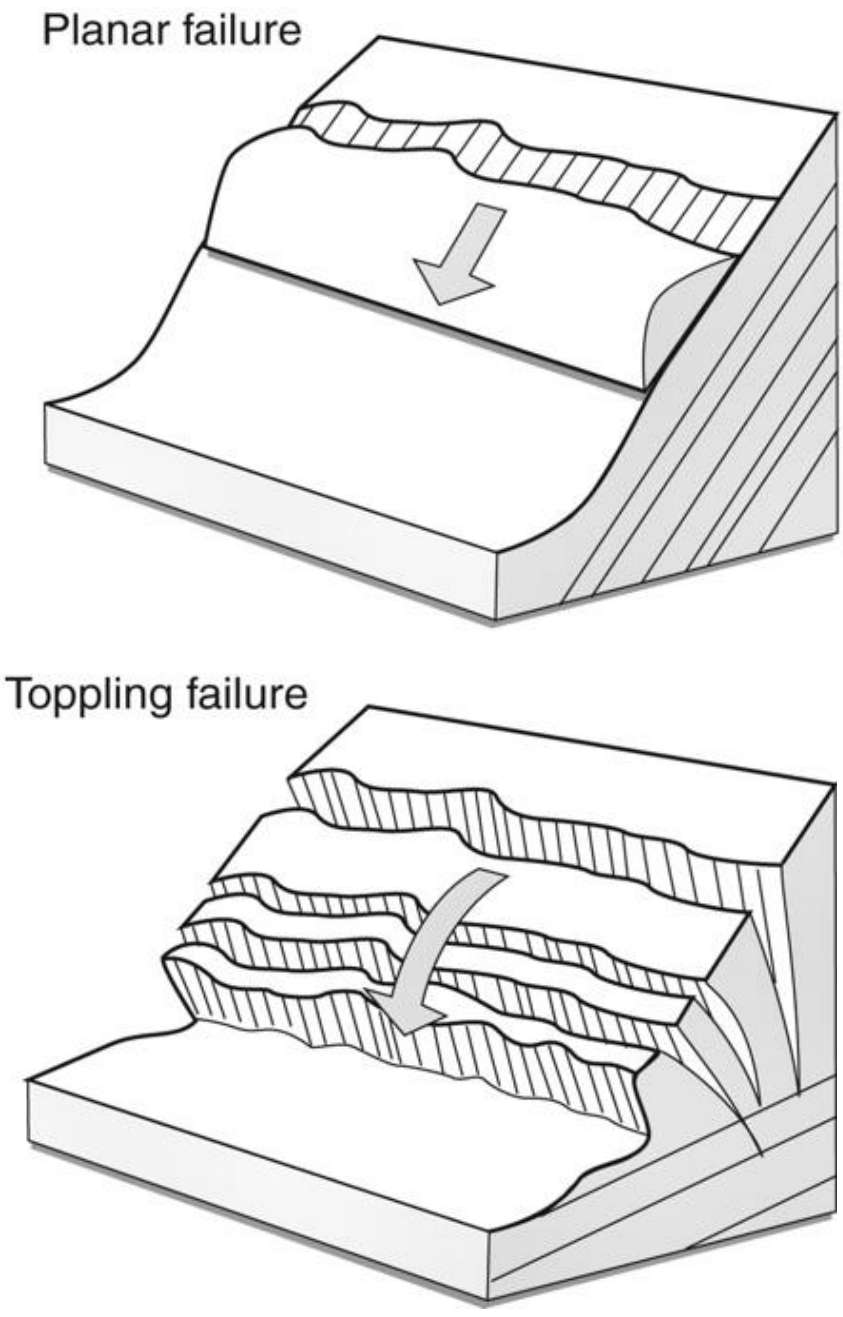

Figure S6. Schematic illustrations displaying planar failure and toppling failure. Figure modified from Hearn (2011).

Appendix F. Oregon Coast Range Mean Roughness Values (LaHusen et al., 2020)

Table S1. Mean roughness values for landslides of known age in the Oregon Coast Range (LaHusen et al., 2020).

Landslide	Roughness (1/m)	Age (Years before 2019)
Little Mill	0.0379	7
NA	0.0197	15
Cummins Peak	0.0226	15
NA	0.0205	249
NA	0.0212	350
Holt Log Res	0.0212	295
Sitkum	0.0154	3000
Drift Creek	0.0195	44
Loon Lake	0.0163	1500
Little Lobster	0.0225	268
Triangle Lake	0.00892	41800
Burchard Lake	0.0205	129
Esmond Lake	0.02	129
Eddy Creek	0.00861	40900